



# A review on mechanisms and recent developments in p-n heterojunctions of 2D materials for gas sensing applications

Minu Mathew<sup>1</sup>, Pratik V. Shinde<sup>1</sup>, Rutuparna Samal<sup>1</sup>, and Chandra Sekhar Rout<sup>1,\*</sup>

<sup>1</sup>Centre for Nano and Material Sciences, Jain University, Jain Global Campus, Jakkasandra, Ramanagaram, Bangalore 562112, India

**Received:** 26 September 2020

**Accepted:** 2 February 2021

**Published online:**

25 February 2021

© The Author(s), under exclusive licence to Springer Science+Business Media, LLC part of Springer Nature 2021

## ABSTRACT

2D materials and their heterojunctions have been explored for gas sensing applications due to their tremendous surface-to-volume ratio, active edges with atomic thickness, and tunable electrical properties. Heterostructures of 2D materials exhibit absolutely novel physics and versatility with accelerated device performance by integrating the atomic scale properties of individual materials. Traditional gas sensors use homogeneous materials as the sensing interface in which the surface adsorbed oxygen ion species play an important role in its performance. But the performance of the sensors suffers greatly due to their selectivity and high working temperature leading to poor stability and short-term uses; the van der Waals 2D p-n heterojunction-based gas sensors hold several advantages since both the materials and the depletion layer formed at the junction can actively tune the sensing performance. By choosing 2D materials with different band structures, charge polarity, carrier concentration, and work function, band alignment at the interface can be precisely engineered to achieve the selective gas sensing performance with low operating temperature. Herein, we have reviewed the working principles, recent developments, and future perspectives of p-n heterojunctions of 2D materials for gas sensing applications.

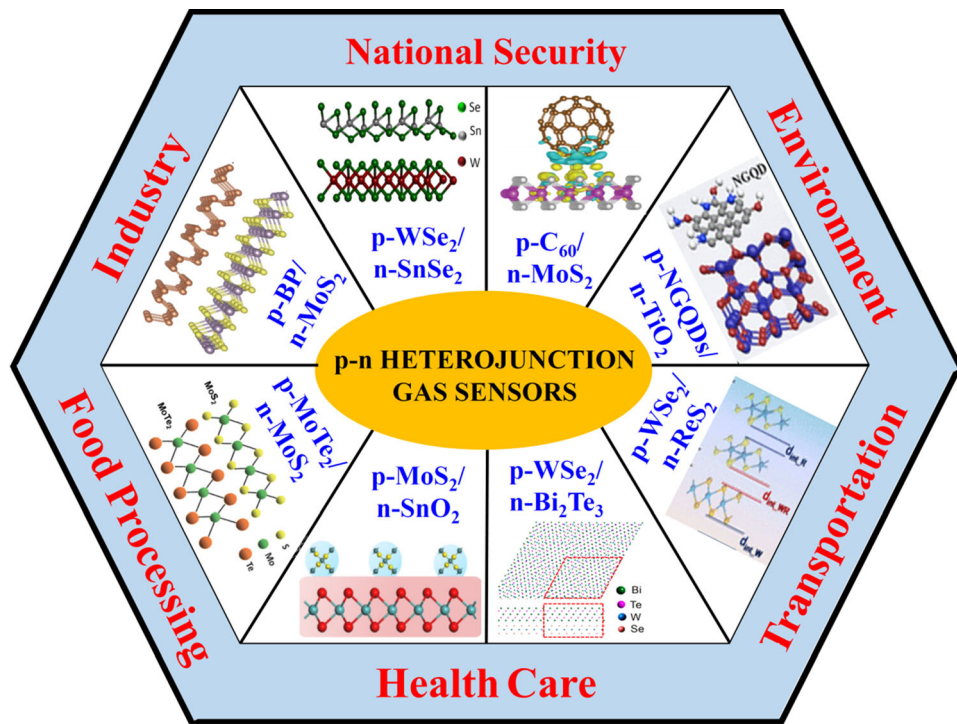
---

Handling Editor: Mark Bissett.

---

Address correspondence to E-mail: r.chandrasekhar@jainuniversity.ac.in; csrout@gmail.com

## GRAPHICAL ABSTRACT



## Introduction

Ultra-thin layered 2D materials have gained tremendous attention in recent years due to their tunable physicochemical properties and wide range of applications in electronics, optoelectronics, chemical sensors, energy storage, conversion devices, etc. [1–6]. 2D materials and their heterojunctions are explored in recent years for chemical and biosensing applications due to their tremendous surface-to-volume ratio, active edges with atomic thickness, and tunable electrical properties. Heterostructures of 2D materials exhibit absolutely novel physics and versatility with accelerated device performance by integrating the atomic scale properties of individual materials [7, 8]. Some of the useful strategies and engineering approaches for the tuning of the properties of the 2D material are phase control, defect creation, doping, alloying, size, and morphology tuning, etc. [9]. Interesting exotic properties are achievable by fabricating n-n, n-p, or p-p

heterojunctions of 2D materials. First discovered by Ohl in 1940, p-n heterojunctions of semiconductors serve as a very important building block for several electronic devices such as rectifier, solar cells, photodetectors, light-emitting diodes, and sensors [10–12]. Due to their novel atomic and crystal structure, 2D nanomaterials offer remarkable flexibility to design p-n junctions with superior performance which is not possible with conventional bulk semiconductors. Also, due to their nanoscale atomic thickness, the carrier concentration, and band alignment of the heterojunctions of 2D materials can be effectively tuned for its possible applications in high-performance electronic devices [13].

Gas sensors have played significant roles in several sectors including oil and gas manufacturing industries, environmental protection, food protection, aerospace, etc. Gas sensors possess several advantages including its easy operation, low-cost fabrication, small size, fast response, etc., compared to other analytical techniques such as gas chromatography-mass spectrometer. The basic requirement for an

efficient and high-performance gas sensor is a high sensitivity, selectivity, response, and recovery times, low operating temperature, and temperature independence and stability in performance, etc. Traditional gas sensors use homogeneous materials as the sensing interface in which the surface adsorbed oxygen ion species play an important role in its performance [14–18]. But the performance of the sensors suffers greatly due to their selectivity and high working temperature leading to poor stability and short-term uses [13, 19]. The van der Waals 2D p-n heterojunction-based gas sensors hold several advantages since both the materials and the depletion layer formed at the junction can actively tune the sensing performance. By choosing 2D materials with different band structures, charge polarity, carrier concentration, and work function, band alignment at the interface can be precisely engineered to achieve the selective gas sensing performance. p-n heterojunction-based gas sensors in which layered 2D material is one of the active components can be classified into two categories based on their fabrication approaches and sensing mechanism: (1) p-n junction diode device-based gas sensors and (2) hybrid p-n heterojunction composite material-based gas sensors. In the first type, fabricated p-n junction diodes are used for the gas sensing by utilizing the properties of the diode in which either a large area film or flakes of 2D materials are used as one of the p- or n-type semiconductor. In the second type of the gas sensor device, the hybrid materials composed of both p- and n-type semiconductor are employed as the active component in which one of the semiconductor materials belongs to the 2D layered material. In this review article, we have provided the basics and working principles of p-n heterojunctions of 2D materials for gas sensing applications. Also, we have reviewed the recent developments and future perspectives of p-n heterojunctions of 2D van der Waals materials for gas sensing applications.

## p-n heterojunctions based on 2D materials

### Types of p-n heterojunctions

A semiconductor p-n heterojunction is formed by interfacing a p-type and an n-type semiconductor material. By this interfacing process, the band bending occurs and the electronic properties get modified

at the interface. This modification can be classified into three different types depending on the band alignment of the two materials taking part in the heterojunction formation (Fig. 1a). The heterostructures are named as type I (Straddling gap), type II (staggered gap), and type III (broken gap), respectively [20, 21]. In heterojunction, the conduction band minimum (CBM) and valence band maximum (VBM) of one material lie fully within the bandgap of other material, and hence, CBM and VBM lie in the same layer. In type II heterojunction, the bandgap of one material partly overlaps with that of the other, with CBM of one of them within the bandgap of the second and resulted in CBM and VBM lying in different layers. In type III heterojunction, CBM and VBM of one material are outside the bandgap of the second, and there is no overlap. In the case of type I heterostructure, the layer with a narrower bandgap forms a well-like structure with the other layer forming a barrier structure. This allows the electrons and holes to get confined which could be formed due to the absorption of photons. Type I heterojunction materials are useful for applications in light-emitting diodes and lasers, etc. Type II heterojunctions are used for photovoltaic devices and photodetectors since the electrons and holes can be spatially well separated with long-lived interlayer excitons. Type III heterojunctions are used in tunneling devices like negative differential resistance (NDR) devices and chemical sensors since p-n junctions can be obtained without external chemical doping.

### Characterization of p-n heterojunctions

Real-world implementation of the heterojunctions devices are now of tremendous demand; however, progress in that direction is harshly affected by the essential technological improvements to produce one kind of semiconductor upper another. The development of diverse growth techniques such as molecular beam epitaxy (MBE) [22, 23], solid/liquid-phase epitaxy (LPE) [24–26], pulsed laser deposition [27], metal organic chemical vapor deposition (MOCVD) [28, 29], hydrothermal [30, 31], solvothermal [32, 33], ultrasonic calcination [34], in situ deposition [35] and several wet chemical methodologies [36] contribute significantly in the fabrication of novel heterojunction devices. Basically, the transition metal dichalcogenides TMDs resembling similar structural properties possesses 2D ultra-thin thickness, morphologies,

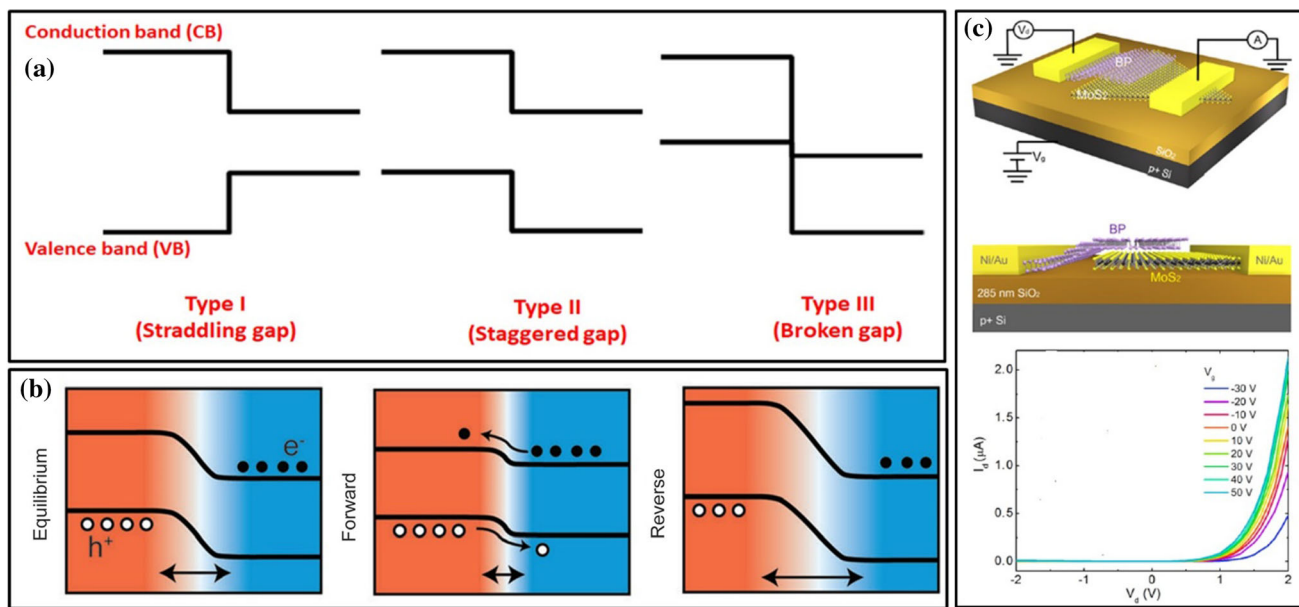


**Figure 1** **a** Different types of heterojunctions formed by p and n-type semiconductors, **b** schematic of the bands in a bulk p–n junction under equilibrium ( $V_{SD} = 0$  V), under forward and reverse bias conditions with the arrow mark indicating the depletion region and change in its width under different conditions. (Source: R. Friesenda, A. J. M. Mendoza, and T. Muller, Atomically thin p–n junctions based on two-dimensional materials, Chem. Soc. Rev. 47, 3339–3358(2018)-Published by the

RSC **c** Representative p–n heterojunction diode based on p-black phosphorous (BP)/n-MoS<sub>2</sub> layers with the I–V characteristics at different gate voltages. (Source: Reprinted with permission from, Y. Deng, Z. Luo, N. J. Conrad, H. Liu, Y. Gong, S. Najmaei, P. M. Ajayan, J. Lou, X. Xu and P. D. Ye, Black Phosphorus–Monolayer MoS<sub>2</sub> van der Waals Heterojunction p–n Diode, ACS Nano 8, 8292–8299 (2014), with permission from Copyright © 2014 American Chemical Society).

remarkable electrical/physical/chemical properties carrying the immense potential for numerous applications [37–39]. These few-layered nanostructures prepared by various synthesis protocols unveil several commendable features enabling them to the appropriate for sensing applications (configuration of logic gates, wearable, and flexible smart electronic sensors) such as wide series of bandgap, high carrier mobility. Properties of heterojunctions reflect prominently with the reduction in layer numbers and thicknesses. The advancements in the fabrication techniques actually help in efficient tuning of different microscopic interface parameters. Manifestation of discrete energy levels results in interesting phenomena; one of them includes resonant tunneling effects. The technology involving p–n heterojunction devices has several parameters such as reverse saturation current, diffusion potential, energy bandgap, forbidden gap, bias voltage, breakdown voltage, nature of the recombination centers can be well characterized by the I–V characteristics. The specific nature and quality of semiconductor p–n junction can be understood by the simplest I–V characterization

method. There is, however, voluminous complementary techniques that provide most crucial conception about defects or impurity (extrinsic) recombination states in the p–n junction. Some of the advanced characterization methods such as cathodoluminescence (CL), electroluminescence (EL), electron beam-induced current (EBIC), scanning electron microscopy (SEM), scanning near field optical microscopy (SNOM), deep-level transient spectroscopy (DLTS), secondary ion mass spectrometry (SIMS), transmission electron microscopy (TEM), electron beam-induced current (EBIC) are summarized below.

Cathodoluminescence and electroluminescence are powerful, expensive, and tedious techniques that utilize electron beams to study the optoelectronic properties. The electron beam initially excites electron–hole pairs and further help in local properties of the region detecting the luminescence radiations. Spatial distribution variation luminescence map depicts the corresponding defect structure distribution in the semiconductor junction. Different resistance distributions and the defect types can be

correlated to luminescence emission wavelengths. The technique yet becomes ineffective to the non-radioactive p-n junctions. Electron beam-induced current mapping technique is attached with SEM or scanning tunneling microscopy (STEM) to analyze minority carrier diffusion lengths and properties of defects in a p-n junction semiconductor. Electron beams scan all over the sample in order to measure the current variations through the p-n junction; the defect states captures the electrons thereby reducing the current value. This method is well applicable to both radiative and non-radiative transitions. Furthermore, NSOM employs optical excitation to scan the defect map signals transmitted through optical fibers in order to convey various contrast mechanisms. Likewise, DLTS is a highly sensitive technique, which reveals deep information regarding electrically active defects buried inside the forbidden gap. The device scans at a constant capacitance value, whereas the defect charge state retrieval roots the capacitance transient according to its population density. TEM, influential microscopic technique, was performed to investigate with atomic-level resolution defect images of the p-n junctions directly. Defect confirmation from TEM imaging is undisputed, because it utilizes minimal amount of sample, making no proper validation of the defects in the entire sample.

SIMS is one of the sensitive surface analysis that uses primary ions to sputter the sample layer, further the secondary ion emission from the uppermost surface carries elemental, crystalline defect as well as the diffusion broadening details of the p-n junctions. Another method calculating doping density and breakdown voltage is capacitance–voltage (C–V) method. However, data interpretations and analysis are found to be complicated in this kind of methodology. Finally, above all these measurements calculating the actual and accurate device characteristics is difficult. p-n junction I–V method is an appropriate method which provide way more sufficient material information for the practical device configuration as well as operation. Recombination is prominent in all semiconductor crystals both is perfect and imperfect systems. Imperfect semiconductor owns excess recombination due to the presence of defects/impurities (traps). The ideal diode equation as derived by Shockley is as follows:

$$J = q \left( \frac{D_N}{L_N} n_{p0} + \frac{D_P}{L_P} p_{n0} \right) \left[ \exp \left( \frac{qV_j}{nKT} \right) - 1 \right] \quad (1)$$

where  $D_N$  and  $D_P$  are the electron and hole diffusion constants,  $n_{p0}$  and  $p_{n0}$  are the equilibrium electron, hole concentrations in the n and p regions,  $L_N$  and  $L_P$  are the Debye lengths for electrons and holes,  $V_j$  is the junction voltage,  $q$  is the magnitude of the electronic charge,  $k$  is the Boltzmann constant, and  $T$  is the temperature. Further the expression for reverse current ( $J_{gen}$ ) and generation current ( $J_R$ ) can be written as:

$$J_{gen} = \frac{qn_i W}{\tau_e} \quad (2)$$

$$J_R = \frac{qn_i^2 \sqrt{D_p}}{N_D \sqrt{\tau_p}} + \frac{qn_i W}{\tau_e} \quad (3)$$

where  $\tau_e$  is the electron recombination time,  $N_D$  is the donor impurity concentration,  $D_p$  is the hole recombination time. Herein, from the above particulars, it is implicit that the I–V characterization is most convenient for understanding the detailed defect states.

### Diode characteristics and fabrication of p-n heterojunctions based on 2D materials

During thermal equilibrium, without an external field, initially, the conduction and valence band edges get lined up, while the Fermi level exhibits a discontinuity at the junction. But the free electrons diffuse from the n-region to the p-region, and similar opposite processes happen for the holes to diffuse from the p-region to the n-region. These flow processes of charges grow until they build an electric field that balances and stops the diffusive flow of carriers Fig. 1b. As a consequence, a space charge region or depletion layer is formed. The width of the depletion region changes under the application of different external voltage (either forward or reverse conditions) as shown in Fig. 1b. The ideal diode equation used for its characterization and evaluation is

$$I_D = I_0 \times \left( e^{\frac{qVD}{\eta kT}} - 1 \right) \quad (4)$$

where  $I_D$  is the current through the diode,  $I_0$  is reverse saturation current,  $V_D$  is the voltage across the diode,  $k$  is Boltzmann's constant,  $\eta$  is ideality factor ( $\eta = 1$  for Si),  $T$  is the temperature in Kelvin,  $q$  is the charge of an electron. A representative p-n

heterojunction diode based on p-black phosphorous (BP)/n-MoS<sub>2</sub> layers and its I-V characteristics at different gate voltages are shown in Fig. 1c.

p-n heterojunctions based on 2D materials can be classified into (1) homojunction (based on a single 2D material), (2) heterojunctions (formed by joining two different 2D materials), and (3) mixed dimensional junctions (based on the combinations of a 2D materials with 0D, 1D, or 3D materials). More elaborated reviews on these topics are reported elsewhere, and the scope of the present review is beyond this topic [40–44]. The p-n heterojunctions based on p-type and n-type 2D semiconductors for applications such as solar cells, light-emitting diodes, and photodetectors have been extensively reviewed in the literature. We have provided summarized information on different p-n junction diodes based on these 2D materials in

Table 1. It is evident from the literature that the p-n heterojunctions based on these 2D materials have emerged as efficient devices for photodetectors, solar cells, lasers, chemical, and gas sensors, etc., due to their tunable functionality. p-n heterostructures of 2D materials can be fabricated by different approaches such as by (1) stacking of two different layered materials by mechanical transfer, (2) one-step or two-step synthesis approaches to growing directly vertical layers substrates or growth of p-n heterojunction composite materials, (3) direct growth of in-plane heterostructure [40–45]. Detailed fabrication methods based on these approaches are discussed and reviewed elsewhere in the literature [40–45].

**Table 1** p-n heterojunctions based on 2D materials

p-n junction	Type	Rectification ratio	V <sub>oc</sub> (V)	Ideality factor	Refs.
p-BP/n-MoS <sub>2</sub>	II	10 <sup>5</sup>	0.3	—	[120]
p-BP/n-MoS <sub>2</sub>	II	28.5	—	—	[121]
p-BP/n-MoS <sub>2</sub>	II	1.5*10 <sup>3</sup>	0.33	2	[122]
p-BP/n-InGaAs	II	4600	—	—	[123]
p-BP/n-ReS <sub>2</sub>	III	10 <sup>6</sup>	—	—	[124]
p-BP/n-ZnO	I	10 <sup>4</sup>	—	1.3	[125]
p-C <sub>60</sub> /n-MoS <sub>2</sub>	II	4*10 <sup>3</sup>	—	—	[126]
p-CuO/n-MoS <sub>2</sub>	II	—	—	—	[127]
p-GaN/n-MoS <sub>2</sub>	I	—	—	—	[128]
p-MoS <sub>2</sub> /n-InSe	II	10 <sup>2</sup>	0.8	2.58	[129]
p-pentacene/n-MoS <sub>2</sub>	II	—	0.3	—	[130]
p-pentacene/n-MoS <sub>2</sub>	II	—	—	2.2 -22.2	[131]
p-(PEA) <sub>2</sub> SnI <sub>4</sub> /MoS <sub>2</sub> /graphene	II	500	—	—	[132]
p-Si/n-MoS <sub>2</sub>	II	5000	0.25	1.83	[133]
p-CuO/n-MoS <sub>2</sub>	II	6000	—	1.37	[134]
p-GaN/n-MoS <sub>2</sub>	II	—	3.2	1.3	[135]
p-GeSe/n-MoS <sub>2</sub>	II	10 <sup>4</sup>	—	—	[136]
p-MoTe <sub>2</sub> /n-MoS <sub>2</sub>	II	4*10 <sup>3</sup>	0.3	1.06–1.34	[137]
p-WSe <sub>2</sub> /n-MoS <sub>2</sub>	II	—	—	1.2	[138]
p-MoSe <sub>2</sub> /n-WS <sub>2</sub>	II	1000	0.72	—	[139]
p-MoTe <sub>2</sub> /n-InGaZnO	II	3*10 <sup>4</sup>	—	1.57	[140]
p-MoTe <sub>2</sub> /n-MoS <sub>2</sub>	II	10 <sup>4</sup>	0.3 V	1.5	[141]
p-Si/n-SnS <sub>2</sub>	II	10 <sup>2</sup>	0.5	—	[142]
p-Si/n-SnSe <sub>2</sub>	II	10 <sup>4</sup>	0.5	1.2	[143]
p-BP/n-WS <sub>2</sub>	II	2.6*10 <sup>4</sup>	0.6	2.3	[144]
p-WSe <sub>2</sub> /n-InGaZnO	II	10 <sup>5</sup>	0.45	1.74	[145]
p-Si/n-WS <sub>2</sub>	II	10 <sup>2</sup>	—	—	[146]
p-BP/n-WSe <sub>2</sub>	I	—	—	1.47	[147]
p-WSe <sub>2</sub> /n-ZnO	II	10 <sup>6</sup>	—	3.4	[148]
p-WSe <sub>2</sub> /n-Bi <sub>2</sub> Te <sub>3</sub>	II	—	0.25	1.55	[149]
p-WSe <sub>2</sub> /n-ReS <sub>2</sub>	II	—	0.64	—	[150]
p-WSe <sub>2</sub> /n-SnSe <sub>2</sub>	II	2*10 <sup>4</sup>	—	—	[151]

## Band alignment prediction techniques and characterization

It is also very important to characterize and understand the alignment of bands of p-type and n-type semiconductors involved in the fabrication of heterojunctions. For the quantification of band offsets in heterojunctions, computational methods, Anderson's model or experimental techniques such as ultraviolet photoelectron spectroscopy (UPS) and X-ray photoelectron spectroscopy (XPS) are employed [46–53]. In this regard, Chiu et al. predicted the bond alignment of heterojunctions based on transition metal dichalcogenides (TMDs) by Anderson's model and experimental techniques such as XPS and UPS [46].

### *Band alignment prediction by Anderson's model*

The electron affinity rule (EAR) which is also known as Anderson's model is based on the principles of electron affinity differences for the two materials involved to form a heterojunction. The conduction band effect (CBO) and the valence bond effect (VBO) of the heterojunctions can be derived from the bandgap differences of the two materials. For example, to find information about the band alignment of 2D materials such as MoS<sub>2</sub>, WSe<sub>2</sub>, and WS<sub>2</sub>, in the first step, the VBM of each individual TMD film is determined by measuring their binding energy using UPS (Fig. 2a). The VBM of the materials with respect to Fermi level (E<sub>F</sub>) as zero points is extrapolated from the UPS data which originates from the  $\Gamma$  point termed as VBM ( $\Gamma$ ). In the second step, VBM ( $\Gamma$ )-E<sub>F</sub> is calculated, and obtained values are found to be 1.44, 1.29, and 1.75 eV, respectively (Fig. 2b). At the same time, the known work function values (WSe<sub>2</sub> = 4.00 eV, MoS<sub>2</sub> = 4.20 eV, and WS<sub>2</sub> = 4.24 eV) which are the energy difference between the vacuum level and E<sub>F</sub> are employed to find information about the band positions and its alignment. By knowing the work function and measuring VBM ( $\Gamma$ )-E<sub>F</sub> values for each TMDs by UPS technique, expected band alignment for the heterojunction can be derived as follows.

For the MoS<sub>2</sub>-WSe<sub>2</sub> and MoS<sub>2</sub>-WS<sub>2</sub> heterojunctions, the predicted VBM ( $\Gamma$ ) are:

$$\begin{aligned}\Delta E_V(\text{MoS}_2 - \text{WSe}_2)_{\text{Predicted}} &= (4.2 \text{ eV} + 1.29 \text{ eV}) \\ &\quad - (4.0 \text{ eV} + 1.44 \text{ eV}) \\ &= 0.05 \text{ eV}\end{aligned}\quad (5)$$

$$\begin{aligned}\Delta E_V(\text{MoS}_2 - \text{WS}_2)_{\text{Predicted}} &= (4.2 \text{ eV} + 1.29 \text{ eV}) \\ &\quad - (4.24 \text{ eV} + 1.75 \text{ eV}) \\ &= -0.5 \text{ eV}\end{aligned}\quad (6)$$

In the third step, the band alignments are predicted by finding the Fermi level differences (Fig. 2c). For the MoS<sub>2</sub>-WSe<sub>2</sub> and MoS<sub>2</sub>-WS<sub>2</sub> heterojunctions, the Fermi level differences are found to be 0.02 and 0.04 eV. Hence, it is predicted that electron charge transfer is expected to happen from WSe<sub>2</sub> to MoS<sub>2</sub> and MoS<sub>2</sub> to WS<sub>2</sub>. Further, the red and blue shifting of the metal core levels of the heterojunctions supported the p-doping and n-doping which supported the predicted band alignment by Anderson's model (Fig. 2d, e).

### *Measurement techniques for band alignment*

The XPS technique is employed to find the binding energy differences between the core levels (Mo3d<sub>5/2</sub>, W4f<sub>7/2</sub>), and VBM ( $\Gamma$ ) of individual TMDs and heterojunction TMD films (Fig. 2 f, g). The band offsets of the TMD heterojunctions are determined by calculating the difference between Mo3d<sub>5/2</sub> and W4f<sub>7/2</sub> for various heterojunctions [46]

$$\begin{aligned}\Delta E_V(\text{MoS}_2 - \text{WSe}_2)_{\text{Expt}} &= (31.61 \text{ eV} + 197.12 \text{ eV}) \\ &\quad - (228.71 \text{ eV}) \\ &= 0.02 \text{ eV}\end{aligned}\quad (7)$$

$$\begin{aligned}\Delta E_V(\text{MoS}_2 - \text{WS}_2)_{\text{Expt}} &= (31.75 \text{ eV} + 196.58 \text{ eV}) \\ &\quad - (228.71 \text{ eV}) \\ &= -0.38 \text{ eV}\end{aligned}\quad (8)$$

By knowing these values, the VBM offsets can be derived which is shown in Fig. 2g. Here the band alignments derived from XPS analysis ( $\Delta E_V(\text{MoS}_2 - \text{WSe}_2)$  &  $\Delta E_V(\text{MoS}_2 - \text{WS}_2)$ ) are 0.02 eV and -0.38 eV which are comparable to the results obtained from Anderson's model. Hence, it is concluded that both Anderson's model and experimental techniques such as XPS and UPS are efficient tools to calculate and understand the band alignment for the 2D material-based p-n heterojunctions.

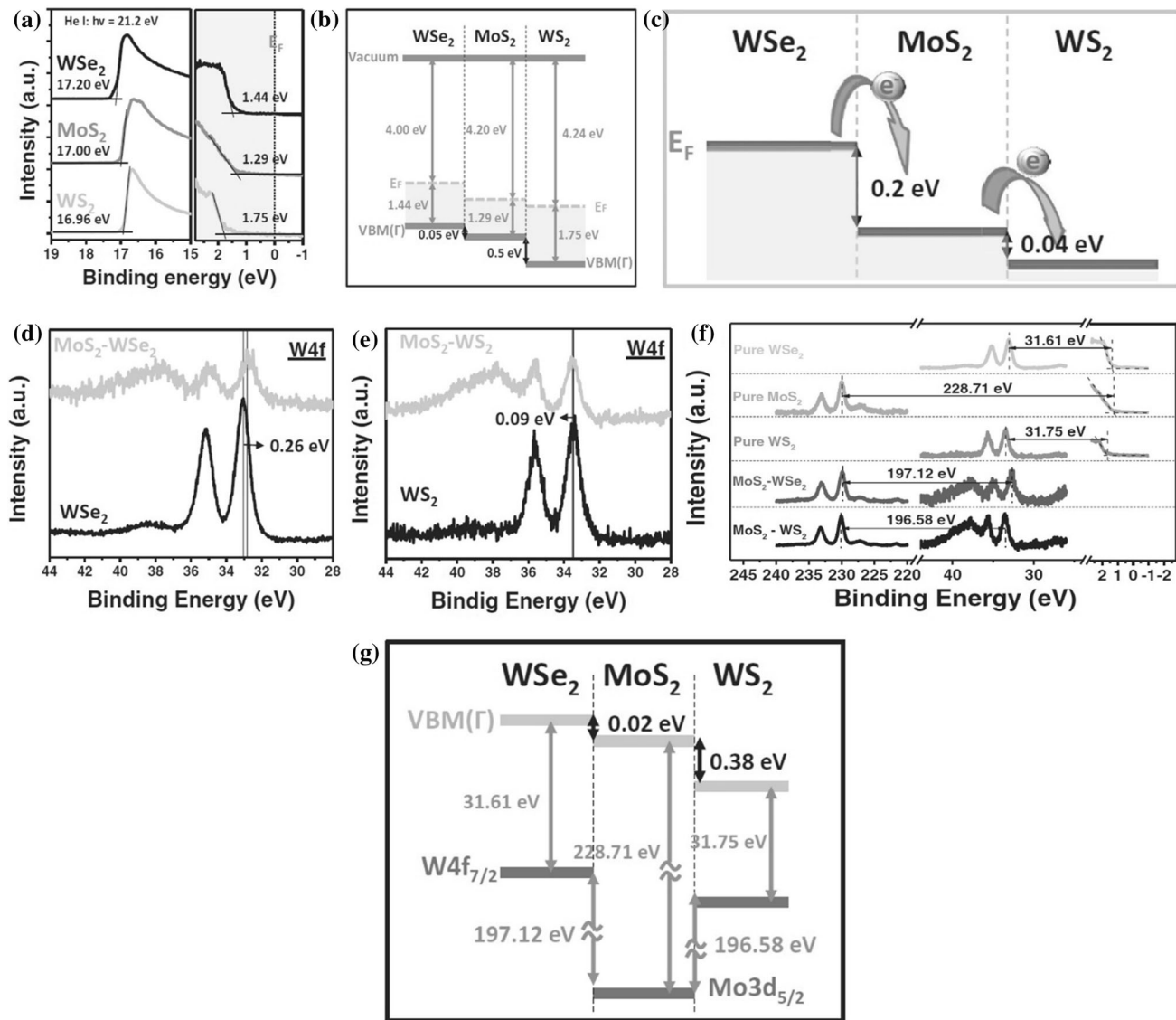


**Figure 2** Band alignment prediction approaches for heterojunctions of 2D materials: **a** UPS spectra of each individual MoS<sub>2</sub>, WS<sub>2</sub>, and WSe<sub>2</sub> films, **b** predicted band alignment among the three TMD films (MoS<sub>2</sub>, WS<sub>2</sub>, and WSe<sub>2</sub>) with Anderson's model, **c** illustration of the predicted charge transfer path when films are contacted, **(d, e)** XPS spectra at W4f before and after MoS<sub>2</sub> stacking on WSe<sub>2</sub> and WS<sub>2</sub>, **f** XPS spectra of the pure MoS<sub>2</sub>, WS<sub>2</sub>, and WSe<sub>2</sub> films, the stacked MoS<sub>2</sub>–

WS<sub>2</sub> and MoS<sub>2</sub>-WSe<sub>2</sub> heterostructures, **g** schematic of the predicted band alignment diagram of the three TMDs. (Source:Reprinted from M.-H. Chiu, W.-H. Tseng, H.-L. Tang, Y.-H. Chang, C.-H. Chen, W.-T. Hsu, W.-H. Chang, C.-I. Wu and L.-J. Li, Band Alignment of 2D Transition Metal Dichalcogenide Heterojunctions, Advanced Functional Materials 27, 1,603,756 (2017) © 2016 WILEY-VCH Verlag GmbH & Co. KGaA, Weinheim).

## General evaluation parameters of gas sensors

The performance of gas sensors is characterized by parameters such as sensor response, sensitivity, response and recovery time, selectivity, detection limit, resolution, and stability [54, 55]

## The sensor response

It (S%) is defined as the ratio between the change in the resistance value of a sensor in the presence and absence of gas molecules with respect to the initial resistance of the sensor.

$$S\% = \frac{R_g - R_{air}}{R_{air}} * 100 \quad (9)$$

where  $R_{\text{air}}$  is the resistance of the sensor in air and  $R_g$  is the resistance of the sensor in the presence of the target gas.

### Sensitivity (S)

It is defined as the change of the measured signal per analyte gas concentration, which can be extracted from the slope of a calibration plot, i.e., a plot of concentration of analyte vs. the electrically measured parameters (resistance, voltage).

### Response and recovery times

These are another key performance indicator of a sensor which is measured in the range from seconds to several tens of minutes. Response time is the time required for the sensor from zero to certain concentration value, and so the recovery time is the time taken by the sensor to return to its initial value. Usually, the response time is the time taken to reach 90% of the full response in the presence of gases, and the recovery time is the time of returning to 90% in the absence of gases.

### The selectivity

The selectivity of a gas sensor determines its capability to detect a certain gas or a specific group of gases in the presence of other gas molecules. Or it is the capability of a sensor to respond to particular gas even in the presence of a gas mixture. Generally, at the same time, sensors can be selected for more than one gas.

### Detection limit

It is the upper and lower limits of detection of the analytes that can be detected by the sensor under given conditions.

### Resolution

It is the lowest concentration difference that can be distinguished by the sensor.

## The stability

of a gas sensor is the ability to deliver reproducible results for the sensor parameters over a certain period of time. It provides important information about the quality and reliable sensor response over time.

## Factors affecting gas sensing of p-n heterojunctions of 2D materials

### Morphological and structural properties of 2D materials

After the successful isolation of graphene, the first 2D material, a lot of research effort has been devoted to the synthesis of other 2D materials. The one or a few layers of atomic planes structure offering astonishing properties in order to perform greatly in several fields such as catalysis, electronic, optoelectronic, high-performance electrodes, nanocomposites, and sensors [56–58]. Compare to bulk crystals, 2D materials provide additional advantages including high surface area, more active sites, facile surface functionalization, good compatibility with device integration, and the possibility to be assembled into 3D architectures. It is possible to fabricate the desired composition, morphology, and functional properties of 2D materials with proper optimization of their synthesis parameters. Moreover, the class of 2D materials shows diverse electronic properties spectra such as metallic, semimetallic, semiconducting, insulating, or superconducting materials based on their chemical composition and structural configuration [59–63]. The capacity of 2D material to identify gas analytes at room temperature offers the possibility for fabricating wearable and flexible gas sensors [64]. In particular, by reducing the structural dimensions to a few nanometers the surface-to-volume ratio is extremely increased, 2D materials provide a large specific surface area and numerous active sites for gas adsorption. This allows the fast charge transferability and tunable physicochemical behavior with the thickness of the material. Increasing the number of gas molecules adsorbed on the nanostructure leads to a strong improvement of the sensitivity of the sensor [65]. Thus, these are attractive candidates for the fabrication of ultra-high-sensitive and low-power gas sensor applications.

## External environment

Other than materials and their nature, the performance of the gas sensor strongly dependent on several environmental parameters such as temperature, humidity, and gas flow rate.

Temperature is one of the most influencing factors on the gas sensor performance, and ideally, the sensor which operates at room temperature is more advantageous in applications. High temperature ( $> 150^{\circ}\text{C}$ ) accelerates the adsorption/desorption processes of gases and increases reactivity between sensing materials and sensitive gases [55]. However, such kind of sensors is unsuitable in some applications, which results in an explosion. Due to the atomically thin layer and available more active sites on the surface, 2D materials are the most attractive materials in gas sensors. This nature allows the fabrications of highly sensitive gas sensors. Korotcenkov et al. showed the performance of a metal oxide-based sensor with respect to operating temperature [66]. According to them, sensor response depends on (1) adsorption of dissociated oxygen at a temperature between  $170^{\circ}\text{C}$  and  $200^{\circ}\text{C}$ , (2) adsorption of (R) molecules converted into RO, (3) desorption of (R), and (4) chemisorbed oxygen desorption.

The sensitivity of gas sensors will be significantly reduced in the presence of water vapors and affects the sensitivity of a sensor for particular or targeted gas. Therefore, to reduce the impact of humidity on sensor performance, it is crucial to design gas sensors that have a very low response to water vapor. There are different types of filters such as powders, porous layers, and membranes are available to remove humidity [54].

The gas flow rate is another important factor influencing the performance of gas sensors. Zhou et al. investigated the gas sensing mechanism of chemiresistors based on rGO [67]. The electric resistance of rGO increases at higher flow rates and decreases for lower flow rates.

## Gas sensing mechanism

### General sensing mechanisms of gas sensors

Gas sensors consist of an active material which detects the analyte gas molecules due to the change in charge carriers of the materials. The gas sensing

performance of a sensor is strictly correlated with the sensing mechanisms. The gas sensing mechanisms of 2D materials and metal oxides are classified into two categories, i.e., (1) surface adsorbed oxygen ions mechanism and (2) charge transfer mechanism. The widely employed surface-adsorbed oxygen ions mechanism involves the surface reaction between the target gas molecules and pre-adsorbed oxygen ions ( $\text{O}_2^-$ ,  $\text{O}^-$ ,  $\text{O}^{2-}$ ) on the surface of the active materials. Depending on the working temperature of the sensor device, a particular type of oxygen ion species is considered to explain the sensing mechanism[15, 68–72].

These oxygen ion species form a depletion layer on the surface of the 2D materials. When the oxygen molecules are adsorbed on the surface of the active materials, they extract electrons from the conduction band and trap the electrons at the surface in the form of ions. This process leads to the band bending and formation of electron depletion or space charge layer. During the exposure of gas molecules (electron-donating or withdrawing), change in the thickness of the depletion layer occurs due to the reaction of the gas molecules with the adsorbed oxygen species and transfer of electrons. The conductivity of the active materials either decreases or increases depending on the p-type and n-type nature of the active sensor material and the type of analyte species, respectively (Fig. 3 a, b).

In the case of the charge transfer mechanism, the charge (electron or hole) transfer occurs between the target analyte gas molecules and the active sensing material (Fig. 3 c,d). Similarly, the direction of charge transfer depends on the oxidizing or reducing nature of the analyte gas [71–73]. The weak or strong interactions depending on the reactivity of the adsorbates and adsorbents result in the modification of the electronic properties of the sensing material and the new transport channels [14, 74]. For example, Yu et al. verified the charge transfer mechanism of  $\text{MoS}_2$ -based sensor for the adsorption of various gas molecules ( $\text{H}_2$ ,  $\text{O}_2$ ,  $\text{H}_2\text{O}$ ,  $\text{NH}_3$ ,  $\text{NO}$ ,  $\text{NO}_2$ , and  $\text{NO}$ ) by first-principles calculations (Fig. 3d) [75].

### Sensing mechanisms of p-n junction diodes and heterojunction material-based gas sensors

In p-n heterojunction-based gas sensor devices, one of the 2D materials acts as a p- or n-type

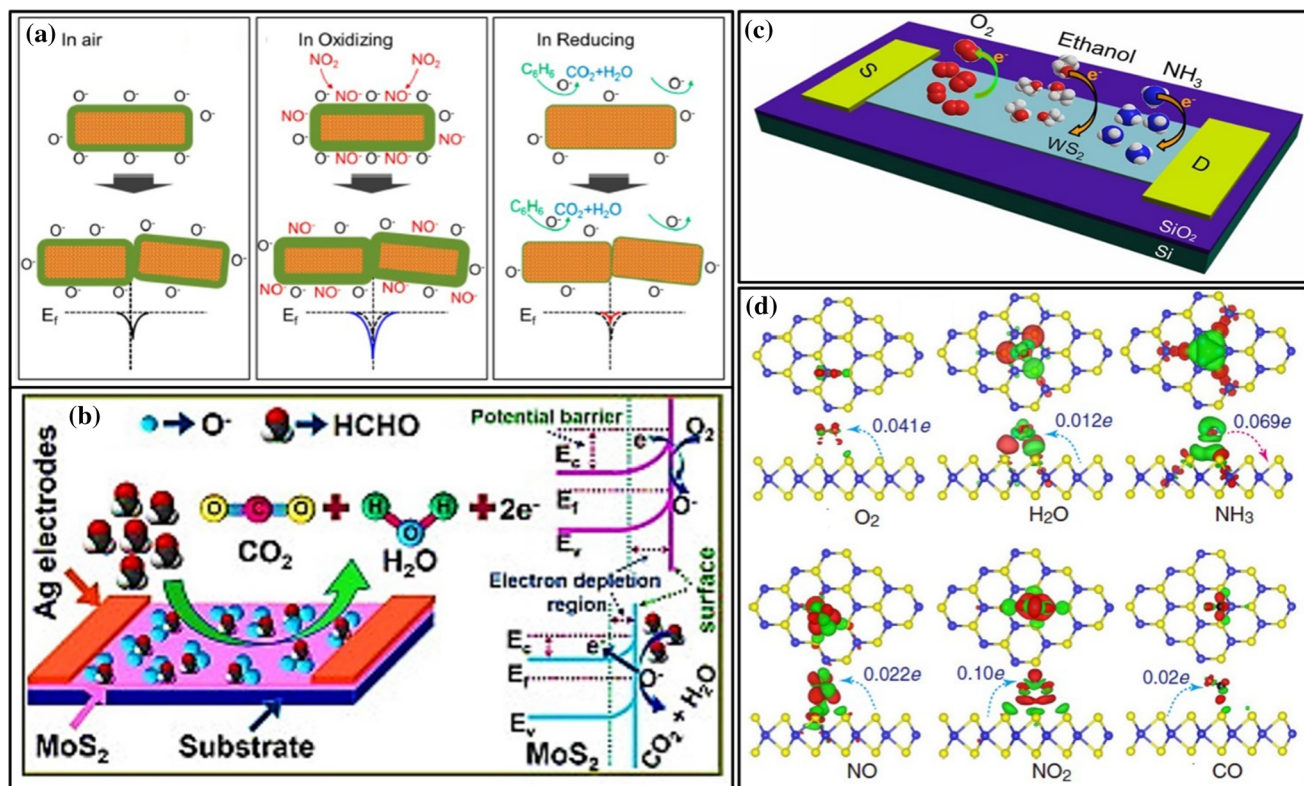


**Figure 3** Schematic Illustration of gas sensing mechanisms in semiconductors for reducing and oxidizing gases: (a, b) Surface adsorbed oxygen ions mechanism( Source: J.-H. Lee, T.-B. Nguyen, D.-K. Nguyen, J.-H. Kim, J.-Y. Kim, B. T. Phan and S. S. Kim, Gas Sensing Properties of Mg-Incorporated Metal-Organic Frameworks, Sensors19, 3323(2019)Source:Reprinted from G. J. Choi, R. K. Mishra and J. S. Gwag, 2D layered  $\text{MoS}_2$ -based gas sensor for indoor pollutant formaldehyde gas sensing

semiconductor to form the junction. The interface region between the two active semiconductors and the interaction of charge carriers at the interface play important roles for the gas sensor performance. Due to the involvement of two semiconducting materials and the interface, the sensor mechanism follows different steps. In the initial step, the spillover mechanism is involved in which atmospheric oxygen molecules capture the conduction band electrons of one of the semiconductors of the p-n junction and form oxygen ions ( $\text{O}_2^-$ ,  $\text{O}^-$ ,  $\text{O}^{2-}$ ) on the surface. These adsorbed oxygen species form the space charge layer at the surface, interface, and junctions of the p-n heterojunctions. At the same time when the p-type and n-type semiconducting layers come in electrical contact, the flow of electrons at the interface takes place from high energy states to unoccupied low-energy states or holes transferred in the opposite

applications, Materials Letters 264, 127,385(2020) with permission from Elsevier) and (c, d) charge transfer mechanism(Source;N. Huo, S. Yang, Z. Wei, S.-S. Li, J.-B. Xia and J. Li, Photoresponsive and Gas Sensing Field-Effect Transistors based on Multilayer  $\text{WS}_2$  Nanoflakes, Sci Rep, 2014, 4, 5209, Source: Reprinted from, Q. Yue, Z. Shao, S. Chang and J. Li, Adsorption of gas molecules on monolayer  $\text{MoS}_2$  and effect of applied electric field, Nanoscale Research Letters8, 425 (2013).

direction until the Fermi levels are equilibrated [13, 19, 76–79]. The flow of carriers stops and a depletion region is formed at the interface when the Fermi levels of the p- and n-type semiconductors are equalized. The change in electron concentration across the junction results in band bending and develops a potential energy barrier at the p-n junction interface [80]. Depending on the analyte gases (oxidizing or reducing) to be detected, the gas molecules release or withdraw electrons to the p-n junction devices. This change in charge carriers of the p-n heterojunctions alters the width of the space charge or depletion layers. Hence, these two factors play an important role in the enhanced sensing performance of p-n heterojunctions of 2D materials. Figure 4 shows a representative schematic illustration of energy band diagrams and band bending of p-n heterojunctions (p- $\text{MoS}_2$ /n- $\text{SnO}_2$  and p- $\text{MoS}_2$ /n-

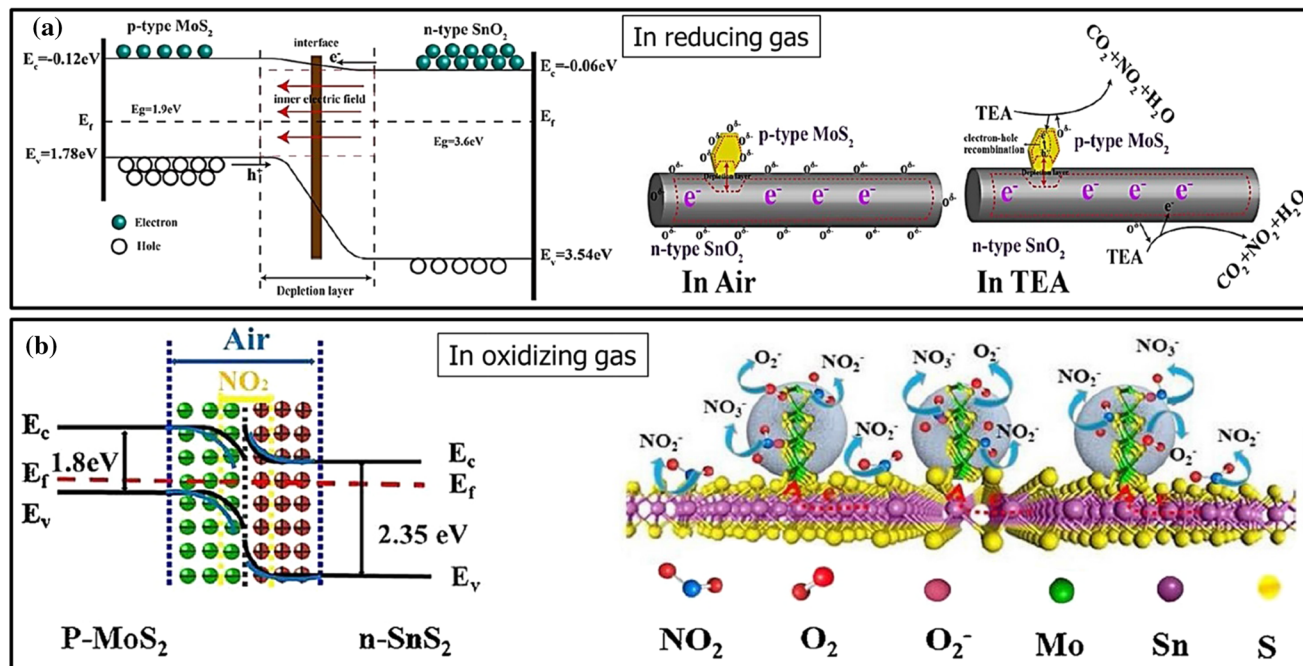
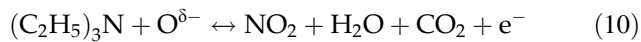


**Figure 4** Schematic illustration explaining the gas sensing mechanisms for the p-n heterojunctions based on 2D materials: **a** Energy band diagrams of MoS<sub>2</sub>/SnO<sub>2</sub> p-n heterojunction in air and in reducing gas vapor (TEA) (Source: Reprinted from X.-Q.Qiao, Z.-W. Zhang, D.-F. Hou, D.-S. Li, Y. Liu, Y.-Q. Lan, J. Zhang, P. Feng and X. Bu, Tunable MoS<sub>2</sub>/SnO<sub>2</sub> P-N Heterojunctions for an Efficient Trimethylamine Gas Sensor and 4-Nitrophenol Reduction Catalyst, ACS Sustainable Chem. Eng.,

2018, **6**, 12,375–12,384, with permission from, Copyright © 2018, American Chemical Society); **b** energy band diagrams of MoS<sub>2</sub>/SnS<sub>2</sub>p-nheterojunction in air and in oxidizing gas (NO<sub>2</sub>) (Source: Reprinted from L. Liu, M. Ikram, L. Ma, X. Zhang, H. Lv, M. Ullah, M. Khan, H. Yu and K. Shi, Edge-exposed MoS<sub>2</sub> nanospheres assembled with SnS<sub>2</sub>nanosheet to boost NO<sub>2</sub> gas sensing at room temperature, Journal of Hazardous Materials **393**, 122,325 (2020) with permission from Elsevier).

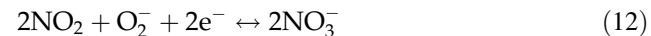
SnS<sub>2</sub>) with sensing mechanisms for reducing (TEA:triethanolamine) and oxidizing (NO<sub>2</sub>) gases respectively [76, 81]. As shown in Fig. 4a, the higher resistance of the MoS<sub>2</sub>/SnO<sub>2</sub> heterojunctions arises due to the formation of the depletion layer and space charge region due to the adsorbed oxygen species near the surface and interface. When the device is contacted with TEA gas molecules the adsorbed oxygen species (O<sup>δ-</sup>: O<sub>2</sub><sup>-</sup>, O<sup>-</sup>, O<sup>2-</sup>) follow the reaction as:



In these processes, excess electrons are released back to SnO<sub>2</sub> resulting in a decrease in resistance. Further, the excess electrons from the TEA molecules release electrons into the p-MoS<sub>2</sub> leading to a decrease in the hole concentration. On the basis of the law of mass action for semiconductors ( $n_0 * p_0 = n_i$ ), the reduction in hole concentration in MoS<sub>2</sub> leads to the increase in electron concentration and results in the decrease of a concentration gradient in the p-n

heterojunctions [76, 81, 82]. These processes help to achieve the reduction in the depletion layer width and barrier height. A similar type of mechanism is followed for other p-n heterojunctions based on 2D materials for the detection of reducing gases.

For the NO<sub>2</sub> sensors based on p-MoS<sub>2</sub>/n-SnS<sub>2</sub>-heterojunction, it is proposed that NO<sub>2</sub><sup>-</sup> and NO<sub>3</sub><sup>-</sup> ion species are formed when NO<sub>2</sub> gas captures free electrons from the acceptor level of the sensor (Fig. 4b).



Accumulation of the NO<sub>2</sub><sup>-</sup>/NO<sub>3</sub><sup>-</sup> at the interface, surface, and near depletion layer of the p-n heterojunction affects the charge transfer in the sensing process [76, 81, 82]. Enhanced sensing performance is achieved for the p-n heterojunctions of 2D material-based sensor due to the modulation of the barrier height induced by the modulation of both the total built-in potential and the ratio between the majority

charge carrier concentrations of both p- and n-type semiconductors [13]. Similar mechanisms are followed for the sensing of oxidizing gases by p-n heterojunctions based on 2D materials.

## Recent developments of gas sensors based on p-n heterojunctions diodes of 2D materials

### TMDs

Single or few layers TMDs have attracted considerable attention because of their tunable band gaps and extensive nature reserves. These compounds show a typical  $MX_2$  formula, where M is an element in Group IV-VI metal, and X is a chalcogen (S, Se, or Te). The layered TMDs are typically 6 to 7 Å thick and consist of an X-M-X hexagonal sandwich with a metal-atomic layer separated by both layers of chalcogen. Due to the excellent sensing and photoelectrical properties of 2D MoS<sub>2</sub>, it is employed for the fabrication of p-n junction-based gas sensors to achieve enhanced performance. Semiconductors have been extensively used as a basic entity in several electronic devices. MoS<sub>2</sub>/Si p-n junctions have several advantages when compared to single MoS<sub>2</sub> material. Mainly, Si semiconductors could be integrated with MoS<sub>2</sub> that having excellent photoelectrical and gas sensing properties for the realization of multifunctional devices. Unique electrical characteristics can be generated by the introduction of a junction area close to the interface. Considering this, Liu et al. investigated electric field tunable and enhanced humidity sensing properties of MoS<sub>2</sub>/Si p-n heterojunction diodes at room temperature [83]. MoS<sub>2</sub> films deposited by dc magnetron sputtering on p-Si substrate exhibited enhanced humidity sensing properties in the forward voltage range and reached a saturated value after  $V = 1.9$  V. A sensitivity of 243.7% is achieved at + 4 V with an increase in current from 1.35 mA to 4.43 mA for 90% RH. Under the bias voltage above + 1.9 V, the interfacial barrier of the p-n junction became narrow, and the sensing performance of the device was completely controlled by MoS<sub>2</sub>. When a reverse bias is applied, the width of the depletion region increased and the charges near the interface are depleted which leads to low humidity sensing performance. Similarly, the n-MoS<sub>2</sub>/p-Si heterojunction showed a high

sensitivity of 769.2% and 19.1% for 9000 ppm and 200 ppm NH<sub>3</sub>, respectively, under the forward condition at 5.0 V [84]. The forward current values increased sharply from 1.3 mA to 11.3 mA at + 5 V in NH<sub>3</sub> ( $S \sim 769.2\%$ ), whereas the reverse current in NH<sub>3</sub> decreased from 29.2 mA to 15.1 mA at -0.4 V with a low response of ~ 48.3%. It is reported that the transport properties of p-n junctions can be tuned by an external electric field and are asymmetric because of the interface band bending. These studies confirmed the enhanced gas sensing performance of heterojunction interface by the incorporation of two or more semiconductors. The comparative sensing performance of different gas sensors based on 2D p-n heterojunction devices are summarized in Table 2. Many of the chemiresistive gas sensors based on n-type (SnO<sub>2</sub>, WO<sub>3</sub>, ZnO) and p-type (CuO, NiO) semiconductor material systems investigated in recent years, could not exhibits the required performance at room temperature. Hence it is highly demanding to develop high-performance gas sensors by exploring new innovative functional gas sensing nanomaterials. MoS<sub>2</sub> is highly demanding candidate for gas sensing due to high surface area, low detection limit owing to 2D layer structure, high mobility, non-toxicity, outstanding mechanical strength, high on-off current ratio and tunable band gap (1.2–1.8 eV). Besides, the 2D nanostructured morphology including nanoworms, nanopetals, and nanosheets own high specific surface area which is advantageous for the development of future nanoelectronic-based gas sensors. It is confirmed that the p-n or n-p heterojunction-based gas sensors are more promising due to their improved gas sensing performance by high modulation in current over the junction. The sensing properties of gas sensor based on MoS<sub>2</sub>/Si p-n heterojunction reported by Liu et al. were not up to the requirement. In order to utilize the performance of ammonia gas sensors at room temperature, Sharma et al. fabricated n-MoS<sub>2</sub>/p-CuO nanoworms thin film-based sensor which provided high sensing response of 47% with fast response/recovery time (17 s/26 s), remarkable reproducibility (15 cycles) and good stability (70 days) during the exposure to 100 ppm NH<sub>3</sub> [80]. The strong adsorption energy of NH<sub>3</sub> molecules as compared to CO and H<sub>2</sub> on the MoS<sub>2</sub> layer demonstrates its superior NH<sub>3</sub> sensing performance [75, 85]. Similarly, NiO/MoS<sub>2</sub>-based p-n junction showed better NH<sub>3</sub> sensing performance when compared to bare NiO and MoS<sub>2</sub> due

**Table 2** Sensing performance of p-n heterojunction diodes based on 2D materials

p-n junction	Analyte gas	Dynamic range	Sensor performance (S = response, $t_{res}$ = response time, $t_{rec}$ = recovery time)	Sensing environment (Environment gas, temperature), RT = Room temperature	References
n-MoS <sub>2</sub> /p-Si	Humidity	30–90% RH	S = 243.7% for 90% RH, $t_{res}$ = 36 s, $t_{rec}$ = 57 s	Air, RT, + 4 V	[83]
n-MoS <sub>2</sub> /p-Si	NH <sub>3</sub>	200–500 ppm	S = 19% for 200 ppm, $t_{res}$ = 5 s, $t_{rec}$ = 5 s	Air, RT, + 5 V	[84]
n-MoS <sub>2</sub> /p-CuO	NH <sub>3</sub>	5–500 ppm	S = 47% for 100 ppm, $t_{res}$ = 17 s, $t_{rec}$ = 26 s	Air, RT	[80]
n-MoS <sub>2</sub> /p-NiO	NH <sub>3</sub>	0.25–50 ppm	S = 63% for 10 ppm, $t_{res}$ = 17 s, $t_{rec}$ = 26 s	Air, RT	[86]
n-graphene/p-TiO <sub>2</sub>	H <sub>2</sub>	0.5–2%	S = 35% for 0.05%, $t_{res}$ = 16 s, $t_{rec}$ = 61 s	125 °C	[152]
n-MoS <sub>2</sub> /p-MoS <sub>2</sub>	NO <sub>2</sub>	8 ppb–100 ppm	S = 100 for 20 ppm, LOD = 8 ppb, $t_{rec}$ = 30 s	Air, RT	[19]
n-MoSe <sub>2</sub> /p-BP	NO <sub>2</sub>	1–500 ppb	S = 10.5% for 25 ppb	Air, RT	[87]
n-ZnO/p-BP	NO <sub>2</sub>	50–150 ppb	S = 74% for 50 ppb	Air, RT	[90]
n-SnS <sub>2</sub> /p-MoS <sub>2</sub>	NO <sub>2</sub>	0.05–100 ppm	S = 25.9% for 100 ppm, $t_{res}$ = 2 s, $t_{rec}$ = 28 s	Air, RT	[81]
n-IGZO/p-WS <sub>2</sub>	NO <sub>2</sub>	1–300 ppm	S = 230% for 5 ppm, LOD = 0.026 ppm	Air, RT	[89]
n-MoS <sub>2</sub> /p-rGO	NO <sub>2</sub>	1–8 ppm	S = 59.8% for 2 ppm,	60 °C	[153]
n-MoS <sub>2</sub> /p-GaN	NO <sub>x</sub>	5–50 ppm	S = 48.42% for 50 ppm, $t_{res}$ = 235 s, $t_{rec}$ = 800 s	Air, RT	[154]

to the availability of much more contact sites and the formation of a depletion layer [86].

Recently, a gas sensor based on mechanically stacked van der Waals p-n junctions of p-type MoS<sub>2</sub> and n-type MoS<sub>2</sub> films was presented by Zheng et al. [84]. The electrical conductivity was greatly influenced by the exposure to NO<sub>2</sub>, superior to most of the early reported studies related to NO<sub>2</sub> sensing. The MoS<sub>2</sub> p-n junction sensor exhibited sensitivity values ~ 60 times higher than the p-type MoS<sub>2</sub> sensor with a low detection limit of 8 ppb, high stability, and high selectivity to NO<sub>2</sub> at room temperature (Fig. 5). The MoS<sub>2</sub> p-n junction sensor showed negligible or no response toward other gases such as NH<sub>3</sub>, formaldehyde, ethanol, acetone, methanol, TEA, etc., confirming its exclusive selectivity to NO<sub>2</sub>. In the process of the formation of the p-n junction, electrons move from n-type MoS<sub>2</sub> to p-type MoS<sub>2</sub> and holes move from p-type MoS<sub>2</sub> to n-type MoS<sub>2</sub> to form the depletion layer and band bending occurs, which

contributed significantly for the sensor performance. p-n heterojunctions based on p-BP/n-MoSe<sub>2</sub> showed 4.4 and 46 times higher NO<sub>2</sub> sensing performance than those of the MoSe<sub>2</sub> and BP FETs, respectively (Fig. 6) [87]. The BP/MoSe<sub>2</sub> heterojunction showed a considerably lower detection limit of 10 ppb as compared to both MoSe<sub>2</sub> (60 ppb) and BP (200 ppb) sensors. In higher NO<sub>2</sub> concentration, the response of the heterojunction and MoS<sub>2</sub> FET showed closer performance due to the dominant Schottky diode type behavior at high concentration [88]. The band alignment at the junction interface could be effectively modulated by the surface adsorbed gas molecules because of 2D materials with atomic thickness, fabricated a highly sensitive gas detector for chemical absorptions. Sensors made of heterojunction demonstrated high sensitivity and lower detection limit toward NO<sub>2</sub>; the enhanced performance was confirmed through Kelvin probe force microscopy and finite element simulations, which are given

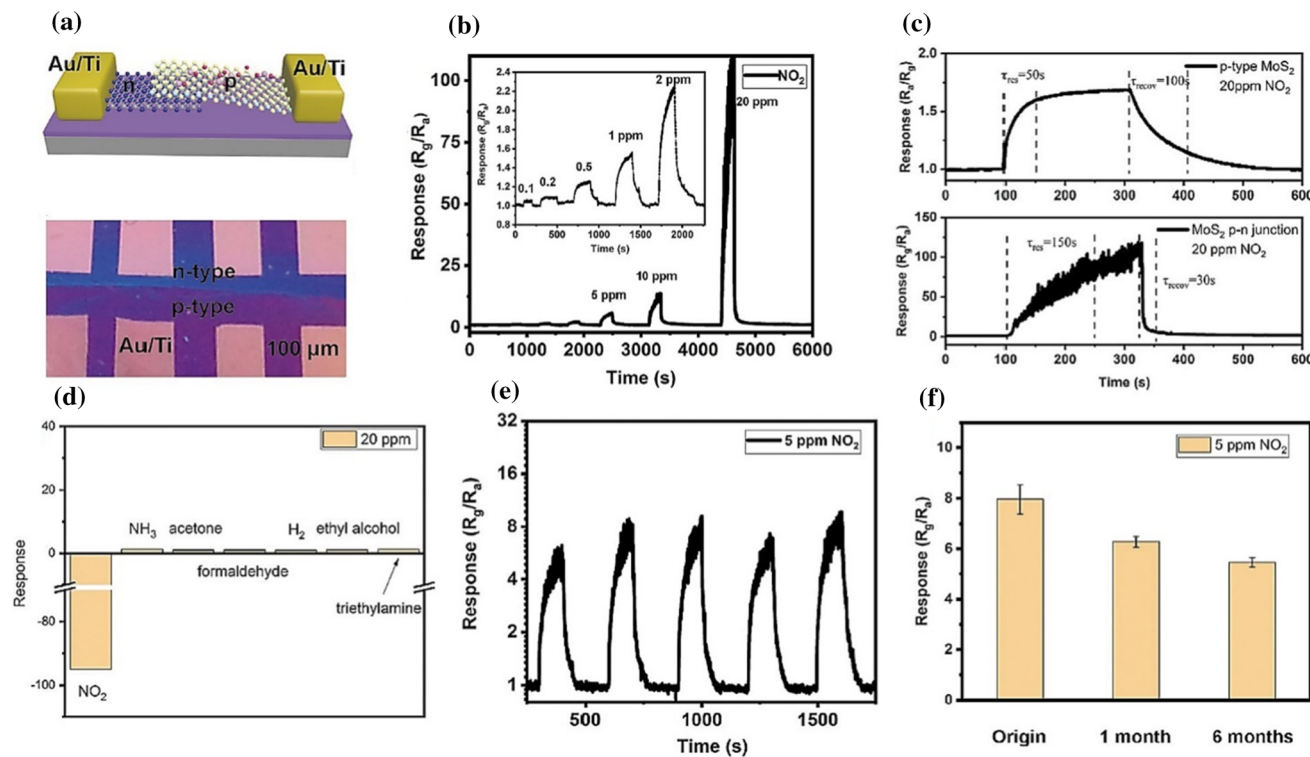


**Figure 5** Gas ( $\text{NO}_2$ ) sensing performance of p-n homojunctions of MoS<sub>2</sub>: (a, b) schematic and optical images of p-n junction, c sensor performance in different concentrations of  $\text{NO}_2$  with inset showing performance at lower concentration, d dynamic response and recovery curves for 20 ppm  $\text{NO}_2$  compared to p-type MoS<sub>2</sub>, e comparative sensing performance in different gases, (f, g)

theoretical and experimental explanations. It revealed crucial changes in carrier transport properties and in-band alignment induced by the chemical absorption. Similarly, p-MoS<sub>2</sub>/n-SnS<sub>2</sub> heterojunctions displayed an excellent response of 25.9 for 100 ppm  $\text{NO}_2$  gas with short response time (2 s) and recovery time (< 30 s) with a low detection limit of 50 ppb and long cycle life at room temperature [81]. Recently, p-WS<sub>2</sub>/n-Indium gallium zinc oxide (IGZO) film fabricated by stacking WS<sub>2</sub> and sputter-deposited IGZO exhibited good  $\text{NO}_2$  sensing performance [89]. The p-n junction diode showed a high  $\text{NO}_2$  sensing response in the range of 1–300 ppm with values of 230% for 5 ppm and 18,170% for 300 ppm [81]. Further, the sensing performance of the p-n diode in the transistor mode could be modulated by the gate bias with sensitivity values of 6820% for 5 ppm and 499,400% for 300 ppm. Also, the sensor device exhibited excellent gas selectivity toward  $\text{NO}_2$  when compared to other gas vapors such as CO,  $\text{NH}_3$ , and humidity. The enhanced sensing performance is attributed due

stability performance of the sensor (Source: Reprinted from W. Zheng, Y. Xu, L. Zheng, C. Yang, N. Pinna, X. Liu and J. Zhang, MoS<sub>2</sub> Van der Waals p-n Junctions Enabling Highly Selective Room-Temperature  $\text{NO}_2$  Sensor, Advanced Functional Materials 30, 2,000,435(2020) with permission from, © 2020 WILEY-VCH Verlag GmbH & Co. KGaA, Weinheim).

to the benefits from the heterojunctions of WS<sub>2</sub> and IGZO and the external electric field under the back gate voltage.

### Black phosphorus

BP is one of the layered 2D materials with a direct bandgap from 0.3 eV(bulk) to 1.5–2.0 eV (monolayer) suitable for charge transfer in optoelectronic devices. Compared to MoS<sub>2</sub> and graphene, BP exhibited smaller out-plane conductivity, larger specific surface area, and stronger adsorption energy, subsequently accelerating its application in gas sensing. Nevertheless, BP alone suffers from insufficient recovery and/or small response. To overcome these challenges, few attempts based on BP-related composites had been demonstrated in recent years. ZnO is widely explored as sensing materials, still suffers challenges including high working temperature, cross-sensitivity, high power consumption, and limited selectivity. To surpass these issues, one

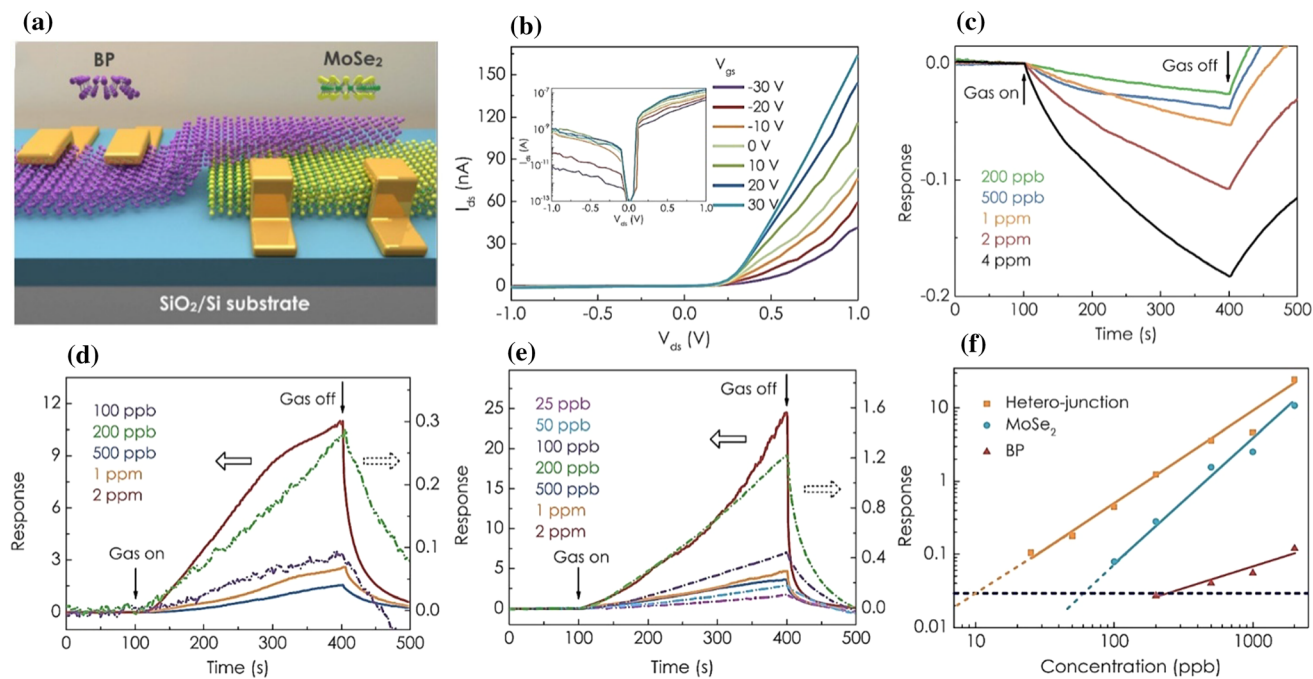


**Figure 6** Gas ( $\text{NO}_2$ ) sensing performance of black phosphorous (BP)/ $\text{MoSe}_2$ p-n heterojunctions: **a** schematic illustration of the device, **b** gate tunable I-V characteristics of the heterojunction. **(c, d, e)** Real-time sensing performance of bare BP,  $\text{MoSe}_2$  and p-n BP/ $\text{MoSe}_2$ heterojunction device, respectively, in different concentrations of  $\text{NO}_2$  with inset showing performance at lower

concentration, **f** comparative sensor performance of the three devices (Source:Reprinted from Z. Feng, B. Chen, S. Qian, L. Xu, L. Feng, Y. Yu, R. Zhang, J. Chen, Q. Li, Q. Li, C. Sun, H. Zhang, J. Liu, W. Pang and D. Zhang, Chemical sensing by band modulation of a black phosphorus/molybdenum diselenide van der Waals hetero-structure, 2D Materials 3, 035,021 (2016).

alternative method is to introduce conducting nano-filters into the host matrix (metal oxide). In this context, Wang et al. reported  $\text{NO}_2$ sensors based on p-BP/n-ZnO with enhanced sensing performance including boosted response (74% vs 37.7% for ZnO toward 50 ppb), accelerated response speed, better long-term stability, and strengthened humidity repelling properties [90]. The enhanced sensing performance was due to the numerous p-n heterojunctions, abundant sorption sites, porous film, and passivation effect of ZnO nanowires on BP nanosheets.

## Recent developments of gas sensors based on p-n heterojunction hybrid materials

### Graphene and TMDs

p-rGO/n-SnS<sub>2</sub>, p-rGO/n-WS<sub>2</sub> heterojunction composites are reported to show good  $\text{NH}_3$  sensing performance which is summarized in Table 3 [91, 92]. The gas sensing behavior of SnS<sub>2</sub> decorated on a

p-type sulfonated r-GO toward  $\text{NH}_3$  was improved 55 times with good stability and minimal fragility to high humidity [91]. Moreover, higher surface energy and the random arrangement of SnS<sub>2</sub> layers on the graphene surface increase the roughness, which made the sensing material superhydrophobic. So, the sensor has shown minimal fragility to high humidity, tending to high stability to different environments. The p-n heterojunction based on SnS<sub>2</sub> and S-rGO greatly modifies the energy band structure; thus, the Schottky barrier height and shifted Fermi level could significantly influence the charge carrier mobility and improved the sensitivity. Besides, the graphene-based gas sensing ink was directly coated on a flexible substrate without IDE, displaying better performance even under mechanical deformation. This ink gives a useful direction for room temperature gas sensing toward various gases, which owns wide applications in environmental monitoring, medical diagnosis, and industrial production. Zhang et al. reported a high-performance flexible p-rGO/n-SnS<sub>2</sub> nanocomposite-based humidity sensor driven by poly(tetrafluoroethylene) triboelectric nano generator

**Table 3** Sensing performance of p-n heterojunction composites based on 2D materials

p-n junction	Analyte gas	Dynamic range	Sensor performance ( $S$ = response, $t_{\text{res}}$ = response time, $t_{\text{rec}}$ = recovery time)	Sensing environment (environment gas, temperature), RT = room temperature	References
p-MoS <sub>2</sub> /n-SnO <sub>2</sub>	TEA	1–200 ppm	$S = 106.3\%$ for 200 ppm at 230 °C	230 °C	[91]
p-NiO/n-gC <sub>3</sub> N <sub>4</sub>	TEA	30–100 ppm	$S = 20.03\%$ for 500 ppm at 280 °C	280 °C	[98]
p-S-rGO/n-SnS <sub>2</sub>	NH <sub>3</sub> NO <sub>2</sub>	1–20 ppm 125 ppb–1 ppm	$S = 11\%$ for 1 ppm $S = 17\%$ for 125 ppb	25–100 °C	[91]
p-rGO/n-WS <sub>2</sub>	NH <sub>3</sub>	10–50 ppm	$S = 256\%$ for 50 ppm, $t_{\text{res}} = 54$ s	RT	[92]
p-rGO/n-In <sub>2</sub> O <sub>3</sub>	NH <sub>3</sub>	1–60 ppm	$S = 95\%$ for 15 ppm, $t_{\text{res}} = 17$ s, $t_{\text{rec}} = 17$ s, LOD ~ 44 ppb	RT	[99]
p-PANI/n-WS <sub>2</sub>	NH <sub>3</sub>	50–200 ppm	$S = 87.2\%$ for 200 ppm	RT	[117]
p-rGO/n-Ni-ZnO	H <sub>2</sub>	1–50 ppm	$S = 29.9\%$ for 50 ppm, $t_{\text{res}} = 80$ s, $t_{\text{rec}} = 180$ s	150 °C	[94]
p-MoS <sub>2</sub> /n-TiO <sub>2</sub>	EtOH	50–700 ppm	$S = 14.2\%$ for 100 ppm	150 °C	[95]
p-rGO/n-SnO <sub>2</sub>	Phenol	10–80 ppb	$S = 1.6\%$ for 60 ppb, LOD ~ 5 ppb, $t_{\text{res}} = 2.4$ s, $t_{\text{rec}} = 1.06$ s	RT	[97]
p-rGO/n-SnS <sub>2</sub>	Humidity	0–97% RH	$t_{\text{res}}/t_{\text{rec}} = 4$ s/3 s for 33% RH and, $t_{\text{res}}/t_{\text{rec}} = 6$ s/15 s for 97% RH	RT	[77]
p-CuPc/n-MoS <sub>2</sub>	Humidity	20–98% RH	0.6/5 MΩ/% RH, $t_{\text{res}} = 50$ s, $t_{\text{rec}} = 25$ s	RT	[155]
p-rGO/n-SnO <sub>2</sub>	NO <sub>2</sub>	25–200 ppm	$S = 14\%$ for 20 ppm, $t_{\text{res}} = 5$ s, $t_{\text{rec}} = 200$ s	RT	[104]
p-rGO/n-SnS <sub>2</sub>	NO <sub>2</sub>	125 ppb–1 ppm	$S = 650\%$ for 1 ppm, $t_{\text{res}} = 75$ s, LOD ~ 1.1 ppb	RT	[93]
p-rGO/n-Fe <sub>3</sub> O <sub>4</sub>	NO <sub>2</sub>	1–50 ppm	$S = 183.1\%$ for 50 ppm	RT	[105]
p-rGO/n-ZnO	NO <sub>2</sub>	10–200 ppm	$S = 8\%$ for 50 ppm	RT	[106]
p-rGO/n-In <sub>2</sub> O <sub>3</sub>	NO <sub>2</sub>	1–200 ppm	$S = 42\%$ for 5 ppm, LOD ~ 2.95 ppb $t_{\text{res}} = 261$ s, $t_{\text{rec}} = 698$ s	50 °C	[107]
p-rGO/n-V <sub>2</sub> O <sub>5</sub>	NO <sub>2</sub>	1–100 ppm	$S = 50.7\%$ for 100 ppm, $t_{\text{res}} = 102$ s, $t_{\text{rec}} = 778$ s	150 °C	[108]
p-BP/n-ZnO	NO <sub>2</sub>	1–500 ppb	$S = 130.7\%$ for 1 ppb, LOD ~ 1 ppb, $t_{\text{res}} = 2$ s, $t_{\text{rec}} = 16$ s	160 °C	[111]
p-SnS/n-SnS <sub>2</sub>	NO <sub>2</sub>	0.125–8 ppm	$S = 660\%$ for 4 ppm	RT	[78]
p-MoS <sub>2</sub> /n-ZnO	NO <sub>2</sub>	25–75 ppb	$S = 63\%$ for 50 ppb, $S = 1.496/\text{ppb}$	60 °C	[156]
p-MoS <sub>2</sub> /n-ZnO	NO <sub>2</sub>	50 ppq–200 ppb	$S = 188\%$ for 200 ppb, LOD ~ 50 ppq ( $10^{-15}$ )	25 °C	[118]
p-MoS <sub>2</sub> /n-SnO <sub>2</sub>	NO <sub>2</sub>	250 ppb–5 ppm	$S = 18.7\%$ for 5 ppm	230 °C	[114]
p-CdTe/n-MoS <sub>2</sub>	NO <sub>2</sub>	0.1–10 ppm	$S = 40\%$ for 10 ppm, $t_{\text{res}} = 26$ s, $t_{\text{rec}} = 114$ s	RT	[116]

**Table 3** continued

p-n junction	Analyte gas	Dynamic range	Sensor performance ( $S$ = response, $t_{\text{res}}$ = response time, $t_{\text{rec}}$ = recovery time)	Sensing environment (environment gas, temperature), RT = room temperature	References
p-NGQDs/n-TiO <sub>2</sub>	NO	10–100 ppm	$S = 12\%$ at RT and 223% at 250 °C for 100 ppm	RT–250 °C	[109]
p-aEG/n-SnS <sub>2</sub>	NO <sub>2</sub>	0.01–100 ppm	$S = 1.04\%$ , LOD $\sim 10$ ppb, $t_{\text{res}} = 0.53$ s, $t_{\text{rec}} = 51.73$ s	RT	[110]

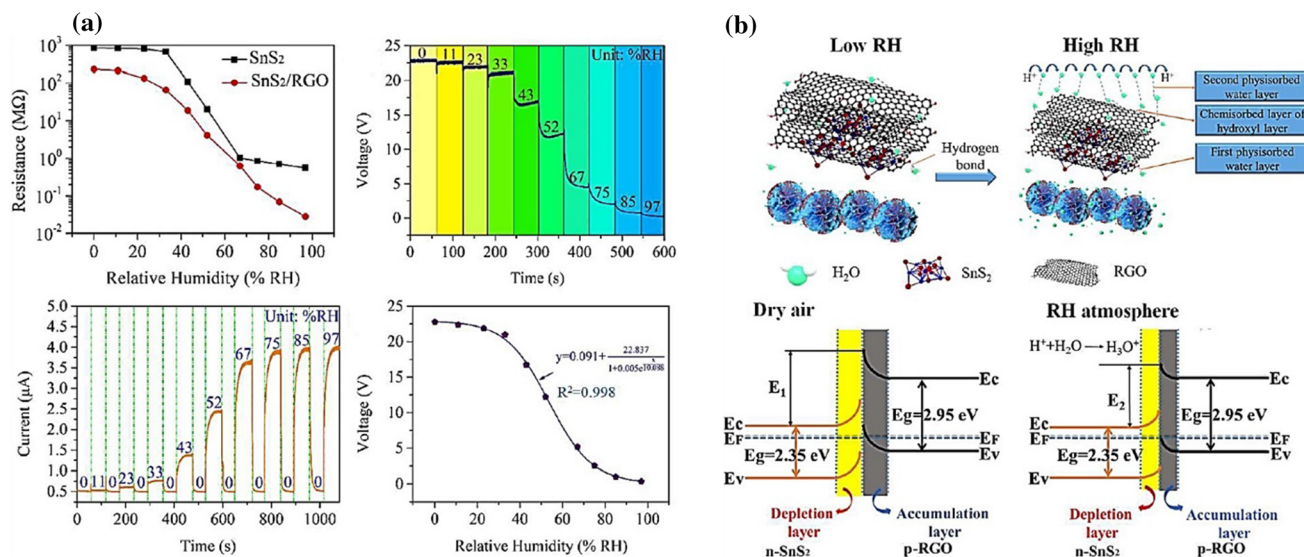


**Figure 7** **a** Humidity sensing performance of p-rGO/n-SnS<sub>2</sub> composite film: change in sensor resistance, the output voltage, output current of the device under various RH and output voltage change as a function of RH. **b** Sensing mechanism of the p-rGO/n-SnS<sub>2</sub> composite film under the exposure of dry air and RH

atmosphere( Source:Reprinted from D. Zhang, Z. Xu, Z. Yang and X. Song, High-performance flexible self-powered tin disulfide nanoflowers/reduced graphene oxide nanohybrid-based humidity sensor driven by triboelectric nanogenerator, Nano Energy 67, 104,251(2020) with permission from Elsevier).

(TENG) for self-powered sensing application (Fig. 7) [77]. The heterojunction material showed good humidity sensing performance with wide sensing range (0–97% RH), fast response/recovery time ( $t_{\text{res}}/t_{\text{rec}} = 4$  s/3 s for 33% RH and,  $t_{\text{res}}/t_{\text{rec}} = 6$  s/15 s for 97% RH, great stability and ultra-low power consumption (29.78  $\mu$ W). This self-powered sensor device demonstrated its capability to monitor human breath with different frequencies, human cough, and finger in various applications for humidity sensing. The change in the depletion layer of the p-n heterojunction determined the humidity sensing performance, which is explained in the schematic band diagram (Fig. 7b). Similarly, Huang et al. presented

heterojunctions based on nanohybrids of SnS<sub>2</sub> and rGO for the detection of NO<sub>2</sub> [93]. By varying the content of rGO, the sensors displayed different responses of p-type and n-type to NO<sub>2</sub>. Both types of NO<sub>2</sub> sensors exhibited good performance with LOD values of 5.03 ppb and 1.10 ppb, sensitivities of 650% and 40% at 1 ppm, fast response and strong selectivity at room temperature. Further, theoretical density functional theory simulations demonstrated that SnS<sub>2</sub> layers enhanced the binding of NO<sub>2</sub> molecules on rGO surfaces and rGO helped to increase the carrier concentration of SnS<sub>2</sub> [93].

## Graphene and metal oxides

The p-n heterostructure nanocomposite materials based on p-rGO/n-Ni-ZnO with 1.6 wt% of rGO (nanosheet/nanowire) showed good H<sub>2</sub> sensing performance [94]. The reason behind the enhanced sensing performance of composite could be explained by two major reasons: (1) formation of the maximum number of p-n heterojunctions with large Schottky barrier height variation for 1.6 wt% rGO and (2) availability of more oxygen ion adsorption sites existing on rGO for H<sub>2</sub> gas. The gas sensing performance was improved in Ni-doped ZnO nanowires due to the availability of more active sites for chemisorbed ionized oxygen atoms. For composites with low concentrations of r-GO, the ZnO sensing mechanism was prominent over the p-n sensing mechanism resulted in a lower response. Similarly, p-n heterojunctions based on p-MoS<sub>2</sub>/n-TiO<sub>2</sub> and p-rGO/n-ZnO also showed better ethanol sensing properties [95, 96]. Guo et al. reported phenol selectivity of p-rGO/n-SnO<sub>2</sub> with LOD as low as 5 ppb when compared to the detection of ethanol, toluene, and methanol [97]. Recently, the composite of p-NiO/n-gC<sub>3</sub>N<sub>4</sub> exhibited good selectivity and response to 500 ppm TEA at 280 °C, which was 3 times higher than the pristine NiO [98]. The highest sensing performance was observed for the composite with 10wt% of n-gC<sub>3</sub>N<sub>4</sub>, by tuning the content of gC<sub>3</sub>N<sub>4</sub> in p-NiO/n-gC<sub>3</sub>N<sub>4</sub>. A flower-like morphology with more active sites was obtained at the relatively low concentration of gC<sub>3</sub>N<sub>4</sub> (< 10 wt%), which is suitable for the surface reaction and thereby leads to enhanced sensing performance. Another composite based on p-rGO/n-In<sub>2</sub>O<sub>3</sub> displayed superior sensing performance to NH<sub>3</sub> at room temperature than the pure materials, with a limit of detection of 44 ppb, a low response time of 17 s, and outstanding selectivity against other nitrogenated compounds and organic solvents. The enhanced NH<sub>3</sub> sensing performance was observed due to the synergic effects resulting from the close interaction between p-rGO and n-In<sub>2</sub>O<sub>3</sub> and the formation of the depletion layer [99].

rGO plays a critical role in several NO<sub>2</sub> sensor device designs due to the availability of abundant adsorption/desorption C-sites and its 2D nature and high surface area. Also, depending on the functional groups present in graphene oxides, it can serve as either p- or n-type and helpful in designing p-n heterojunction composite materials [100–103]. By

utilizing the advantages of p-rGO, its p-n heterojunctions such as p-rGO/n-SnO<sub>2</sub>, p-rGO/n-SnS<sub>2</sub>, p-rGO/n-Fe<sub>3</sub>O<sub>4</sub>, p-rGO/n-ZnO, p-rGO/n-In<sub>2</sub>O<sub>3</sub>, p-rGO/n-V<sub>2</sub>O<sub>5</sub>, graphene/TiO<sub>2</sub>, etc., are investigated for NO<sub>2</sub> sensing applications which are summarized in Table 3 [93, 104–110]. p-n heterojunctions based on Metal oxide/rGO have been extensively used to synthesize room temperature gas sensors owing to improved carrier separation efficiency at the interface and RGO nanosheets with large specific surface areas. But the complete exploration of metal oxide/RGO is limited because of the sheet stacking of RGO nanosheets. Considering this, Zhou et al. reported that 3D core-shell rGO/Fe<sub>3</sub>O<sub>4</sub>p-n junctions exhibited good selectivity, high sensitivity of 183.1% for 50 ppm NO<sub>2</sub> and LOD of 50 ppb which was about 8.17 times higher than the pure bare materials [105]. The 3D core-shell structure inhibited agglomeration during RGO reduction and could give more active sites than 2D RGO due to the higher surface area. In addition to p-n junction, the sensing performance is also promoted by the synergic interaction between Fe<sub>3</sub>O<sub>4</sub> and RGO. It could be concluded that the formed heterojunctions facilitate carrier transport and further improve the gas sensing properties. While the high carrier transport of RGO provide fast and smooth channels for carrier transfer, which accelerates fast response of the sensor. In<sub>2</sub>O<sub>3</sub> is one of the most promising and conventional sensing materials but the practical applications is restricted due to the higher working temperature. To overcome this problem, rGO has been explored as critical sensing material owing to its large number of defects and dangling bonds. By considering all these facts, p-rGO/n-In<sub>2</sub>O<sub>3</sub> heterojunction nanofibers with an optimized amount of rGO (2.2 wt%) exhibited a response of 42 to 5 ppm NO<sub>2</sub> at a low operating temperature of 50 °C, which was 4.4 times higher than that of pristine In<sub>2</sub>O<sub>3</sub> [107]. The enhanced sensing performance is attributed due to the formation of p-n heterojunctions between rGO and In<sub>2</sub>O<sub>3</sub> and ultra-high surface area as well as the strong gas adsorption capacity of rGO nanosheets [107].

## p-n heterojunctions based on other 2D materials (Black phosphorus, TMDs, Metal chalcogenides)

Phosphorene has been known to be a promising material for gas sensing because of its excellent

carrier mobility, high chemical activity, and ultra-high surface volume ratio. Considering these aspects, Li et al. fabricated hollow spheres of p-BP/n-ZnO heterojunction composites, showing significantly high NO<sub>2</sub> sensing performance with an ultra-low detection limit down to 1 ppb, high response, outstanding selectivity, faster response, and recovery dynamic process [111]. The existence of BP helped to achieve a high surface area-to-volume ratio and increased the local chemical affinity of BP, leading to the enhanced NO<sub>2</sub> sensing performance. Optimal p-n heterostructures based on p-SnS/n-SnS<sub>2</sub> is reported to show ultra-sensitive NO<sub>2</sub> sensing performance at room temperature due to the formation of the electron accumulation layer in the junction [78]. The heterojunction sensor exhibited a response value of 660% for 4 ppm NO<sub>2</sub>, excellent selectivity, LOD of 0.075 ppm and reliable long-term stability for four months (Fig. 8).

The sensing performance of p-SnS/n-SnS<sub>2</sub> is studied for the room temperature detection of NO<sub>2</sub> due to the increased adsorption sites, enhanced electron transfer, and the larger resistance modulation. The formation of heterojunctions based on SnS<sub>2</sub>/SnS led

to the accumulation of multiple NO<sub>2</sub> molecules and affected the charge transfer process significantly during the sensing process (Fig. 8b). The interfaces act as highly active sites because of the presence of sulfur defects, vacancies, and lattice misfit, appropriate for the adsorption of NO<sub>2</sub> and NO<sub>2</sub><sup>-</sup> between the surface atoms of SnS<sub>2</sub> and SnS [78, 112, 113].

The practical applications of MoS<sub>2</sub>-based gas sensors are hindered because of poor recoverability and insufficient sensitivity. To overcome these obstacles, Han et al. developed a p-MoS<sub>2</sub>/n-SnO<sub>2</sub>-based sensor for the detection of NO<sub>2</sub> at room temperature, with a response value of 18.7 for 5 ppm NO<sub>2</sub>, reliable long-term stability for 4 weeks, and outstanding selectivity at room temperature [114]. Meanwhile a p-MoS<sub>2</sub>/n-ZnO heterojunction having mass ratio of 1:2 exhibited an optimal NO<sub>2</sub> sensing performance at 60 °C with a response of 63% toward 50 ppb, the sensitivity of 1.496/ppb, excellent repeatability, and good selectivity [115]. The excellent sensing properties are exhibited due to the formation of numerous p-n heterojunctions and unique combination of nanostructures. Recently, Jaiswal et al. studied NO<sub>2</sub> sensing properties of p-CdTe (quantum dots)/n-MoS<sub>2</sub>

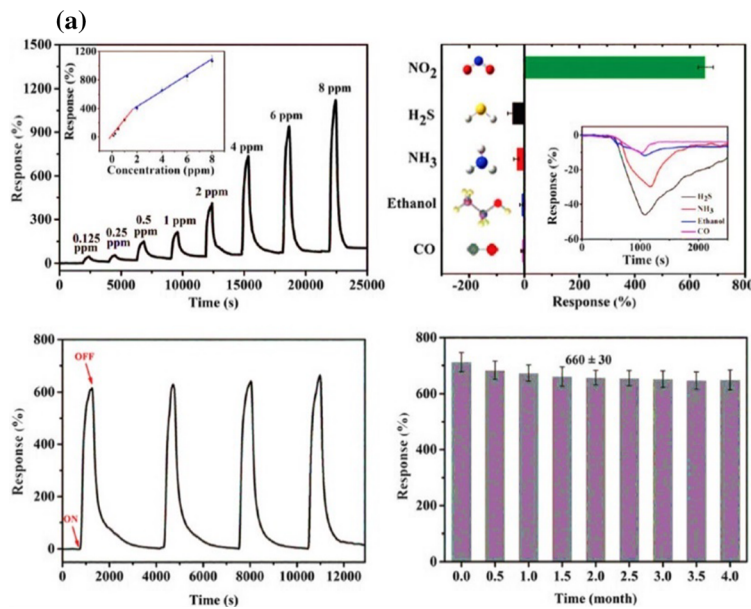
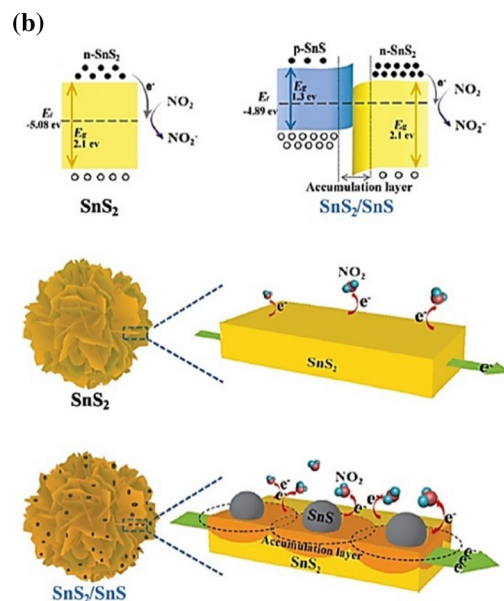


**Figure 8** **a** Gas (NO<sub>2</sub>) sensing performance of p-SnS/n-SnS<sub>2</sub> heterojunctions: dynamic sensor response of the device in 0.125 to 8 ppm NO<sub>2</sub> at room, sensing responses of the sensor to 4 ppm of various gases, including H<sub>2</sub>S, NH<sub>3</sub>, CO, and ethanol, four successive sensing cycles of the sensor to 4 ppm NO<sub>2</sub> and aging test toward 4 ppm NO<sub>2</sub> for 4 months. **b** Scheme of the gas sensing mechanism with band structures of the SnS<sub>2</sub> (left) and SnS<sub>2</sub>/SnS



(right) gas sensors after absorption of NO<sub>2</sub> molecules, respectively and Corresponding models of the gas sensing process( Source:Reprinted from Q. Sun, J. Wang, J. Hao, S. Zheng, P. Wan, T. Wang, H. Fang and Y. Wang, SnS<sub>2</sub>/SnS p-n heterojunctions with an accumulation layer for ultra-sensitive room temperature NO<sub>2</sub> detection, *Nanoscale* 11, 13,741–13,749 (2019) with permission from RSC).

(nanoworms) heterojunctions [116]. The superior gas sensing performance is attributed to several factors including hybrid heterostructure with unique morphology, catalytic activity, synergistic effects, and p-n heterojunctions. The hybrid p-CdTe/n-MoS<sub>2</sub> heterojunction thin-film sensor device showed high sensor response (40%), fast response time ~ 16 s, recovery time ~ 114 s, and high selectivity toward 10 ppm NO<sub>2</sub> at room temperature compared to the pristine MoS<sub>2</sub> thin-film sensor (sensor response ~ 26%, response time ~ 23 s, incomplete recovery). Similarly, the synergistic effects of n-WS<sub>2</sub> nanosheets in a PANI matrix helped to achieve high-performance NH<sub>3</sub> sensing properties in terms of its selectivity, high response, low detection limit, shorter response, and recovery times at room temperature [117]. The construction of p-n heterojunctions offered a versatile solution to surpass the complexities of 2D material-based gas sensors and also paved a new way for room temperature sensor applications.

### Tuning the sensor performance of the p-n junction of 2D materials by a different approach

The gas sensing performance of p-n heterojunctions based on 2D materials can be further improved by different approaches including UV light irradiation, defect engineering, doping, tuning by the external gate voltage, by attaching functional groups, etc.[81, 85, 87, 89, 90]. UV irradiation helps to reduce the p-n junction barrier, charge transfer due to the better Fermi level alignment between the p-n junction, production of excess photogenerated carriers and favor to overcome the Schottky barrier and participation of more charge carriers in the gas sensing process[19, 81, 87]. Figure 9a, b, c, d, e, f summarizes the UV irradiation effect on a p-MoS<sub>2</sub>/n-MoS<sub>2</sub>-heterojunction NO<sub>2</sub> sensor device. Zheng et al. reported 60 times improved sensitivity of p-n heterojunction to 20 ppm NO<sub>2</sub> as compared to the p-type MoS<sub>2</sub> with a LOD of 8 ppb and fast recovery time within 30 s. Under UV illumination, a much-improved sensor response of 188% toward 20 ppb NO<sub>2</sub> with a full recovery as compared to the tiny response of 40% and incomplete recovery for 10 ppm NO<sub>2</sub> in dark conditions.

Similarly, by tuning the transport characteristics of p-n heterojunctions, enhanced gas sensing

performance can be achieved (Fig. 9 g, h, j, k, l). Band shape and barrier height of the heterojunction can be effectively modulated by applying an external back gate voltage which is summarized in Fig. 9 for a p-WS<sub>2</sub>/n-IGZnO based NO<sub>2</sub> sensor [79, 119]. Tang et al. demonstrated that NO<sub>2</sub> (300 ppm) sensor response of 4,99,400% can be achieved after applying -20 V gate bias as compared to a maximum response of 18,170% on its chemiresistor mode[79].

### Conclusion and future directions

2D graphene and its layered inorganic analogs are promising materials for gas sensing applications due to their exceptional chemical and physical properties. Intrinsic rGO, GO, and graphene are excellent candidates for the highly sensitive detection of gases at room temperature with low detection limits and reversibility. Besides, the other layered 2D materials such as metal oxides, h-BN, phosphorene, TMDs, III-IV semiconductors, etc., have a high surface area, tunable bandgaps, semiconducting property making them suitable candidates for gas sensing applications. Recently, research is focussed on the development of p-n heterojunctions based on 2D materials to improve the sensing performance by combining the properties of different 2D materials. The various p-n heterojunctions based on 2D materials open a new research era, and the band alignment by heterojunction formation provides the possibility to develop novel devices with desired characteristics and potential energy-related applications. Because of the difference in the performance of component materials, the heterojunction is a wide choice for gas sensing applications and is known to be cost-effective and its synthesis is relatively simple. The unique surface characteristics of 2D materials and the number of possibilities for fabricating them with other suitable dimensional materials make them a better choice for manufacturing several gas sensor architectures. Adopting the prominent properties of their component materials, p-n heterojunction-based devices were developed for comprehensive gas sensing applications.

In spite of these various advantages, gas sensors composed of 2D material-based p-n heterojunctions still face challenges. In view of their larger lateral size, 2D nanostructured materials extend superior conformal contact with the electrodes, yet the large-

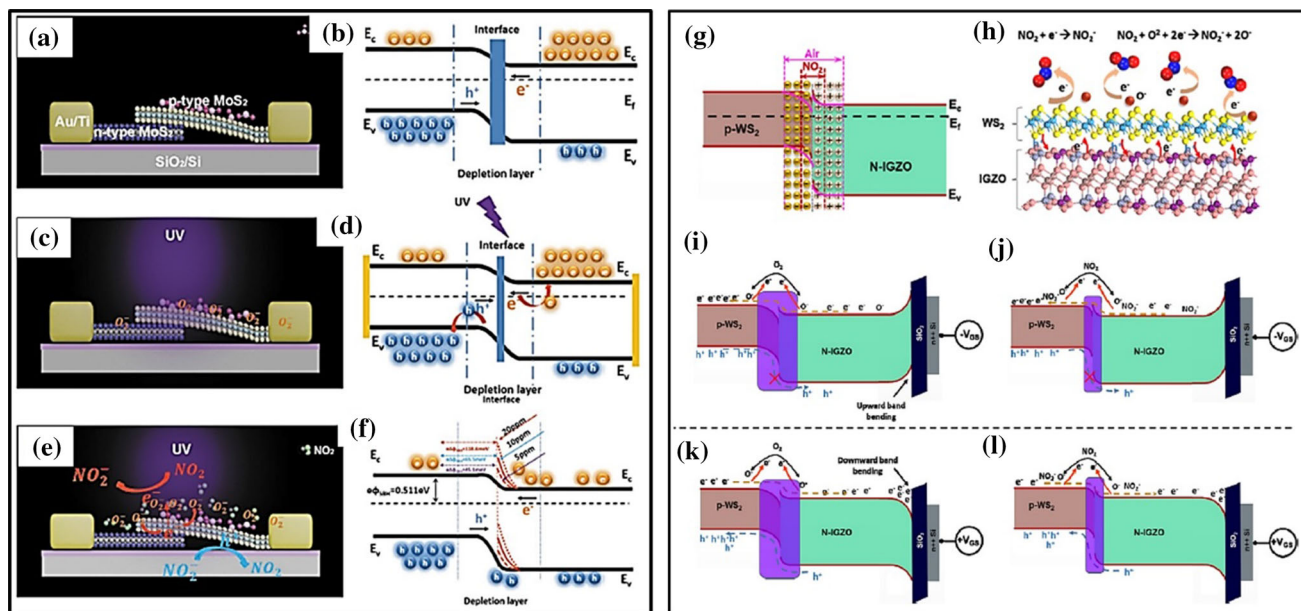


**Figure 9** Tuning the gas sensing performance of p-n heterojunctions by UV irradiation: Schematic structures of MoS<sub>2</sub> p-n junction in **a** dark, **c** under UV irradiation, **e** exposed to NO<sub>2</sub> gas under UV irradiation. (**b**, **d**, **f**) Energy band diagrams of the MoS<sub>2</sub> p-n junction in dark, under UV irradiation, and p-n junction under UV irradiation with change in Schottky barrier height (SBH) for NO<sub>2</sub> concentrations of 5, 10, and 20 ppm respectively. Tuning the gas sensing performance by applied gate voltage: (**g**) energy band structure of p-WS<sub>2</sub>/n-IGZO heterojunction in air and NO<sub>2</sub> atmosphere, (**h**) sensing mechanism (**Source**: Reprinted from W. Zheng, Y. Xu, L. Zheng, C. Yang, N. Pinna, X. Liu and J. Zhang, MoS<sub>2</sub> Van der Waals p–n Junctions Enabling Highly Selective

Room-Temperature NO<sub>2</sub> Sensor, Advanced Functional Materials **30**, 2,000,435(2020) with permission from, © 2020 WILEY-VCH Verlag GmbH & Co. KGaA, Weinheim). The band diagram of p-WS<sub>2</sub>/n-IGZO heterojunction in (**i**) air (**j**) NO<sub>2</sub> after applying negative gate voltage, (**k**, **l**) after applying positive gate voltage in air and NO<sub>2</sub> respectively (**Source**: Reprinted from H. Tang, Y. Li, R. Sokolovskij, L. Sacco, H. Zheng, H. Ye, H. Yu, X. Fan, H. Tian, T.-L. Ren and G. Zhang, Ultra-High Sensitive NO<sub>2</sub> Gas Sensor Based on Tunable Polarity Transport in CVD-WS<sub>2</sub>/IGZO p-N Heterojunction, ACS Appl. Mater. Interfaces **11**, 40,850–40,859(2019) with permission from, Copyright © 2019 American Chemical Society).

scale synthesis of high-quality 2D layered nanostructured materials left overs significant limitations. Further efforts should be made to commission the large-scale preparation of p-n heterojunctions gas sensor devices by understanding the growth mechanism of 2D layered nanostructured materials. The optimized synthesis of 2D nanostructures with suitable surface morphological modification can open higher sensing capabilities of the device. The influence of gas mixtures, environment, humidity, etc., on the performance of the sensor must be quantified and controlled, yet it is not clearly understood. To date, most of the sensors have a detection limit in parts per billion (ppb) or just slightly under that. So, there is a need for crucial development in order to achieve the detection limit in parts-per-trillion levels. Another challenge to overcome is the selective detection performance of the sensor for certain types of gas. The ability to differentiate particular gas from a mixture

of gas must be improved. The gas sensors comprised of 2D materials greatly influenced by the adsorbed gas molecules but faced to electrical instability and long recovery time under variant surroundings. In future, more attention is needed on surpassing the limitations such as material instability, low detection limit, sensitivity, selectivity, removal of contaminants that are affecting the performance level of the sensors. The potential of these sensors in economical, large-scale applications such as to detect environmental hazards and gases yet are not well explored. There is a need for more practical and theoretical combined studies, which represent a thorough understanding of the gas sensors.

By selecting appropriate 2D nanostructured materials with different work functions and band gaps, the band alignment at the interface could be effectively controlled to enhance their sensing and selectivity performance. The gas sensors can attain

outstanding sensitivity and very low detection limits through the incorporation of UV light to remove the unwanted impurities. Another approach is to improve the detection limits by adding dopants or creating defects/hybrids as it promotes better interaction via charge transfer between the gas molecules and the modified 2D materials. Generally, morphology and a good nanostructure play a crucial role in gas sensing applications and can be even considered to be responsible for excellent performance including the selectivity and high response. The appropriate optimization of the available various approaches will help to enhance gas sensing performance.

Self-powered gas sensors are promising to fabricate as smart implantable devices for various sensing applications with unique properties and advantages over the classic chemical sensors. However, self-powered gas sensors based on p-n heterostructures comprised of 2D materials are needed to be studied more in order to realize the practical implementations and have a crucial role in future sensing network for several fields. Besides, a self-powered gas sensor can be an economical and technological driver for developing flexible gas sensor industries. The combination of gas sensing characteristics with piezoelectric properties can be fabricated into an epidermal gas sensing system. It is because the close contact of the human body with the piezoelectric network during body motion would generate a piezoelectric signal for driving gas sensors without the assistance of an external power source. Moreover, mechanical tolerance and sensing performance improved by the manufacturing of sensor devices with different geometries (crumpled, serpentine, and buckled) via geometrical engineering. The self-healing ability of flexible e-skin gas sensors is inevitable for further enhancement in lifetime and reliability after several accidental breakage and mechanical deformations over time. However, there are technological and scientific gaps for further developments to realize their full potential at a real-time sensing platform. So, a futuristic multi-disciplinary approach is needed to surpass the existing scientific gaps confronted by flexible and wearable gas sensors based on p-n heterostructures of 2D materials. Moreover, the growing demand for flexible, transparent, and energy-efficient devices has inspired the scientific research community to look into the exciting physics of these gas sensor devices by exploring ultra-thin functional materials.

## Acknowledgements

This work was financially supported by the Department of Science and Technology (DST)-SERB Early Career Research project (Grant No. ECR/2017/001850), DST-Nanomission (DST/NM/NT/2019/205(G), DST/TDT/SHRI-34/2018), Karnataka Science and Technology Promotion Society (KSTePS/VGST-RGS-F/2018-19/GRD NO. 829/315).

## Compliance with ethical standards

**Conflict of interest** The authors declare no conflict of interest.

## References

- [1] Xu J, Zhang J, Zhang W, Lee C-S (2017) Interlayer nanoarchitectonics of two-dimensional transition-metal dichalcogenides nanosheets for energy storage and conversion applications. *Adv Energy Mater* 7:1700571. <https://doi.org/10.1002/aenm.201700571>
- [2] Island JO, Molina-Mendoza AJ, Barawi M et al (2017) Electronics and optoelectronics of quasi-1D layered transition metal trichalcogenides. *2D Mater* 4:022003. <https://doi.org/10.1088/2053-1583/aa6ca6>
- [3] Dai J, Li M, Zeng XC (2016) Group IVB transition metal trichalcogenides: a new class of 2D layered materials beyond graphene. *WIREs Comput Mol Sci* 6:211–222. <https://doi.org/10.1002/wcms.1243>
- [4] Potje-Kamloth K (2008) Semiconductor junction gas sensors. *Chem Rev* 108:367–399. <https://doi.org/10.1021/cr0681086>
- [5] Miller DR, Akbar SA, Morris PA (2014) Nanoscale metal oxide-based heterojunctions for gas sensing: a review. *Sens Actuators B Chem* 204:250–272. <https://doi.org/10.1016/j.snb.2014.07.074>
- [6] Wang Z, Nayak PK, Caraveo-Frescas JA, Alshareef HN (2016) Recent developments in p-type oxide semiconductor materials and devices. *Adv Mater Weinheim* 28:3831–3892. <https://doi.org/10.1002/adma.201503080>
- [7] Zhou X, Hu X, Yu J et al (2018) 2D layered material-based van der Waals heterostructures for optoelectronics. *Adv Func Mater* 28:1706587. <https://doi.org/10.1002/adfm.201706587>
- [8] Jin H, Guo C, Liu X et al (2018) Emerging two-dimensional nanomaterials for electrocatalysis. *Chem Rev* 118:6337–6408

- [9] Zhu Y, Peng L, Fang Z et al (2018) Structural engineering of 2D nanomaterials for energy storage and catalysis. *Adv Mater Weinheim* 30(15):1706347
- [10] Ohl RS (1948) Light-sensitive electric device including silicon, US2443542A, 15, 1948
- [11] Riordan M, Hoddeson L (1997) The origins of the p-n junction. *IEEE Spectr* 34(6):46–51. <https://doi.org/10.1109/6.591664>
- [12] Frisenda R, Mendoza AJM, Mueller T (2018) “Atomically thin p–n junctions based on two-dimensional materials.” *Chem Soc Rev* 47:3339–3358
- [13] Feng Z, Chen B, Shuangbei Q (2016) Chemical sensing by band modulation of a black phosphorus/molybdenum diselenide van der Waals hetero-structure. *2D Mater* 3(3):035021
- [14] Kannan PK, Late DJ, Morgan H, Rout CS (2015) Recent developments in 2D layered inorganic nanomaterials for sensing. *Nanoscale* 7:13293–13312. <https://doi.org/10.1039/C5NR03633J>
- [15] Zhang L, Khan K, Zou J (2019) Recent advances in emerging 2D material-based gas sensors: potential in disease diagnosis. *Adv Mater Interfaces* 6:1901329
- [16] Hashtroudi H, Mackinnon IDR, Shafiei M (2020) Emerging 2D hybrid nanomaterials: towards enhanced sensitive and selective conductometric gas sensors at room temperature. *J Mater Chem C* 8:13108–13126
- [17] Huang Y, Guo J, Kang Y, Yi A, Li CM (2015) Two dimensional atomically thin MoS<sub>2</sub> nanosheets and their sensing applications. *Nanoscale* 7(46):19358–19376
- [18] Lee E, Yoon YS, Kim DJ (2020) Two-dimensional transition metal dichalcogenides and metal oxide hybrids for gas sensing. *ACS Sens.* <https://pubs.acs.org/doi/10.1021/acssensors.8b01077>. Accessed 18 Aug 2020
- [19] Zheng W, Xu Y, Zheng L et al (2020) MoS<sub>2</sub> Van der Waals p–n junctions enabling highly selective room-temperature NO<sub>2</sub> sensor. *Adv Func Mater* 30:2000435. <https://doi.org/10.1002/adfm.202000435>
- [20] Milnes AG (1972) Heterojunctions and metal semiconductor junctions. 1st Edition. <https://www.elsevier.com/books/heterojunctions-and-metal-semiconductor-junctions/p-418>
- [21] S. M. Sze and K. K. Ng, (2010) Transferred-electron device. In: Complete guide to semiconductor devices. John Wiley & Sons, Ltd, pp 64–74
- [22] Henck H, Ben Aziza Z, Zill O et al (2017) Interface dipole and band bending in the hybrid \$p\backslash ensuremath{-}n\$ heterojunction \$\mathrm{Mo}\{\mathrm{S}\}\_{2}\mathrm{GaN}(0001)\$. *Phys Rev B* 96:115312. <https://doi.org/10.1103/PhysRevB.96.115312>
- [23] Lanius M, Kampmeier J, Weyrich C et al (2016) P-N junctions in ultrathin topological insulator Sb<sub>2</sub>Te<sub>3</sub>/Bi<sub>2</sub>Te<sub>3</sub> heterostructures grown by molecular beam epitaxy. *Cryst Growth Des* 16:2057–2061. <https://doi.org/10.1021/acs.cgd.5b01717>
- [24] Song Z, Schultz T, Ding Z et al (2017) Electronic properties of a 1D intrinsic/p-doped heterojunction in a 2D transition metal dichalcogenide semiconductor. *ACS Nano* 11:9128–9135. <https://doi.org/10.1021/acsnano.7b03953>
- [25] Wang H, Liu F, Fu W et al (2014) Two-dimensional heterostructures: fabrication, characterization, and application. *Nanoscale* 6:12250–12272. <https://doi.org/10.1039/C4NR03435J>
- [26] Ohta H, Mizoguchi H, Hirano M et al (2003) Fabrication and characterization of heteroepitaxial p–n junction diode composed of wide-gap oxide semiconductors p-ZnRh<sub>2</sub>O<sub>4</sub>/n-ZnO. *Appl Phys Lett* 82:823–825. <https://doi.org/10.1063/1.1544436>
- [27] Ohta H, Hirano M, Nakahara K et al (2003) Fabrication and photoresponse of a pn-heterojunction diode composed of transparent oxide semiconductors, p-NiO and n-ZnO. *Appl Phys Lett* 83:1029–1031. <https://doi.org/10.1063/1.1598624>
- [28] Montes J, Yang C, Fu H et al (2019) Demonstration of mechanically exfoliated \$\beta\$-Ga<sub>2</sub>O<sub>3</sub>/GaN p–n heterojunction. *Appl Phys Lett* 114:162103. <https://doi.org/10.1063/1.5088516>
- [29] Ruzmetov D, Neupane MR, Herzing A et al (2018) Van der Waals interfaces in epitaxial vertical metal/2D/3D semiconductor heterojunctions of monolayer MoS<sub>2</sub> and GaN. *2D Mater* 5:045016. <https://doi.org/10.1088/2053-1583/aad1b7>
- [30] Fei W, Gao J, Li N et al (2021) A visible-light active p–n heterojunction NiFe-LDH/Co<sub>3</sub>O<sub>4</sub> supported on Ni foam as photoanode for photoelectrocatalytic removal of contaminants. *J Hazard Mater* 402:123515. <https://doi.org/10.1016/j.jhazmat.2020.123515>
- [31] Jiang T, Cheng L, Han Y et al (2020) One-pot hydrothermal synthesis of Bi<sub>2</sub>O<sub>3</sub>-WO<sub>3</sub> p–n heterojunction film for photoelectrocatalytic degradation of norfloxacin. *Sep Purif Technol* 238:116428. <https://doi.org/10.1016/j.seppur.2019.116428>
- [32] Shi W, Li M, Huang X et al (2020) Construction of CuBi<sub>2</sub>O<sub>4</sub>/Bi<sub>2</sub>MoO<sub>6</sub> p–n heterojunction with nanosheets-on-microrods structure for improved photocatalytic activity towards broad-spectrum antibiotics degradation. *Chem Eng J* 394:125009. <https://doi.org/10.1016/j.cej.2020.125009>
- [33] Wang S, Zhao L, Huang W et al (2021) Solvothermal synthesis of CoO/BiVO<sub>4</sub> p–n heterojunction with micro-nano spherical structure for enhanced visible light

- photocatalytic activity towards degradation of tetracycline. *Mater Res Bull* 135:111161. <https://doi.org/10.1016/j.materesbull.2020.111161>
- [34] Pirhashemi M, Habibi-Yangjeh A (2018) Fabrication of novel ZnO/MnWO<sub>4</sub> nanocomposites with p-n heterojunction: visible-light-induced photocatalysts with substantially improved activity and durability. *J Mater Sci Technol* 34:1891–1901. <https://doi.org/10.1016/j.jmst.2018.01.014>
- [35] Xiao Y, Peng Z, Zhang W et al (2019) Self-assembly of Ag<sub>2</sub>O quantum dots on the surface of ZnIn<sub>2</sub>S<sub>4</sub> nanosheets to fabricate p-n heterojunctions with wonderful bifunctional photocatalytic performance. *Appl Surf Sci* 494:519–531. <https://doi.org/10.1016/j.apsusc.2019.07.175>
- [36] Shi G, Zhang X, Li J et al (2017) Fabrication of 3D biomimetic composite coating with broadband antireflection, superhydrophilicity, and double p-n heterojunctions. *Nano Res* 10:2377–2385. <https://doi.org/10.1007/s12274-017-1434-5>
- [37] Samal R, Rout CS (2020) Recent developments on emerging properties, growth approaches, and advanced applications of metallic 2D layered vanadium dichalcogenides. *Adv Mater Interfaces* 7:1901682. <https://doi.org/10.1002/admi.201901682>
- [38] Niu R, Han R, Wang Y et al (2021) MXene-based porous and robust 2D/2D hybrid architectures with dispersed Li<sub>3</sub>Ti<sub>2</sub>(PO<sub>4</sub>)<sub>3</sub> as superior anodes for lithium-ion battery. *Chem Eng J* 405:127049. <https://doi.org/10.1016/j.cej.2020.127049>
- [39] Li X, Fu Y, Ding X et al (2021) Magnetically controlled 2D nano-DNA fluorescent biosensor for selective and sensitive detection of alkaline phosphatase activity. *Sens Actuators B Chem* 327:128914. <https://doi.org/10.1016/j.snb.2020.128914>
- [40] Frisenda R, J. Molina-Mendoza A, Mueller T, et al (2018) Atomically thin p–n junctions based on two-dimensional materials. *Chem Soc Rev* 47:3339–3358. <https://doi.org/10.1039/C7CS00880E>
- [41] Wang J, Verzhbitskiy I, Eda G (2018) Electroluminescent devices based on 2D semiconducting transition metal dichalcogenides. *Adv Mater Weinheim* 30:e1802687. <https://doi.org/10.1002/adma.201802687>
- [42] Zeng Q, Liu Z (2018) Novel optoelectronic devices: transition-metal-dichalcogenide-based 2D heterostructures. *Adv Electron Mater* 4:1700335. <https://doi.org/10.1002/aem.201700335>
- [43] Li M-Y, Chen C-H, Shi Y, Li L-J (2016) Heterostructures based on two-dimensional layered materials and their potential applications. *Mater Today* 19:322–335. <https://doi.org/10.1016/j.mat tod.2015.11.003>
- [44] Wang J, Li Z, Chen H et al (2019) Recent advances in 2D lateral heterostructures. *Nano-Micro Lett* 11:48. <https://doi.org/10.1007/s40820-019-0276-y>
- [45] He Q, Liu Y, Tan C et al (2019) Quest for p-type two-dimensional semiconductors. *ACS Nano* 13:12294–12300. <https://doi.org/10.1021/acsnano.9b07618>
- [46] Chiu M-H, Tseng W-H, Tang H-L et al (2017) Band alignment of 2D transition metal dichalcogenide heterojunctions. *Adv Func Mater* 27:1603756. <https://doi.org/10.1002/adfm.201603756>
- [47] Kang J, Tongay S, Zhou J et al (2013) Band offsets and heterostructures of two-dimensional semiconductors. *Appl Phys Lett* 102:012111. <https://doi.org/10.1063/1.4774090>
- [48] Komsa H-P, Krasheninnikov AV (2013) Electronic structures and optical properties of realistic transition metal dichalcogenide heterostructures from first principles. *Phys Rev B* 88:085318. <https://doi.org/10.1103/PhysRevB.88.085318>
- [49] Liang Y, Huang S, Soklaski R, Yang L (2013) Quasiparticle band-edge energy and band offsets of monolayer of molybdenum and tungsten chalcogenides. *Appl Phys Lett* 103:042106. <https://doi.org/10.1063/1.4816517>
- [50] Gong C, Zhang H, Wang W et al (2013) Band alignment of two-dimensional transition metal dichalcogenides: application in tunnel field effect transistors. *Appl Phys Lett* 103:053513. <https://doi.org/10.1063/1.4817409>
- [51] Guo Y, Robertson J (2016) Band engineering in transition metal dichalcogenides: stacked versus lateral heterostructures. *Appl Phys Lett* 108:233104. <https://doi.org/10.1063/1.4953169>
- [52] Rasmussen FA, Thygesen KS (2015) Computational 2D materials database: electronic structure of transition-metal dichalcogenides and oxides. *J Phys Chem C* 119:13169–13183. <https://doi.org/10.1021/acs.jpcc.5b02950>
- [53] Chiu M-H, Zhang C, Shiu H-W et al (2015) Determination of band alignment in the single-layer MoS<sub>2</sub>/WSe<sub>2</sub> heterojunction. *Nat Commun* 6:7666. <https://doi.org/10.1038/ncomms8666>
- [54] Rajkumar K, Kumar RTR (2019) Chapter 6 - gas sensors based on two-dimensional materials and its mechanisms. In: Hywel M, Rout CS, Late DJ (eds) Fundamentals and sensing applications of 2D materials. Woodhead Publishing, Cambridge
- [55] Bochenkov VE, Sergeev GB (2010) Sensitivity, selectivity, and stability of gas-sensitive metal-oxide nanostructures, metal oxides and their applications. In: Umar A, Hahn Y-B (eds) Metal Oxide Nanostructures and their applications, vol. 3. American Scientific Publishers, pp. 31–52

- [56] Umar A, Ammar HY, Kumar R et al (2020) Efficient H<sub>2</sub> gas sensor based on 2D SnO<sub>2</sub> disks: experimental and theoretical studies. *Int J Hydrogen Energy* 45:26388–26401. <https://doi.org/10.1016/j.ijhydene.2019.04.269>
- [57] Arash A, Ahmed T, Rajan AG et al (2019) Large-area synthesis of 2D MoO<sub>3-x</sub> for enhanced optoelectronic applications. *2D Mater* 6:035031. <https://doi.org/10.1088/2053-1583/ab1114>
- [58] Li S, Wang S, Salamone MM et al (2017) Edge-enriched 2D MoS<sub>2</sub> thin films grown by chemical vapor deposition for enhanced catalytic performance. *ACS Catal* 7:877–886. <https://doi.org/10.1021/acscatal.6b02663>
- [59] Jiao Y, Hafez AM, Cao D et al (2018) Metallic MoS<sub>2</sub> for high performance energy storage and energy conversion. *Small* 14:1800640. <https://doi.org/10.1002/smll.201800640>
- [60] Gul HZ, Sakong W, Ji H et al (2019) Semimetallic graphene for infrared sensing. *ACS Appl Mater Interfaces* 11:19565–19571. <https://doi.org/10.1021/acsmami.9b00977>
- [61] Ding Q, Czech KJ, Zhao Y et al (2017) Basal-plane ligand functionalization on semiconducting 2H-MoS<sub>2</sub> monolayers. *ACS Appl Mater Interfaces* 9:12734–12742. <https://doi.org/10.1021/acsmami.7b01262>
- [62] Chikkoor G, Karanam SP, Star S et al (2018) Hexagonal boron nitride: the thinnest insulating barrier to microbial corrosion. *ACS Nano* 12:2242–2252. <https://doi.org/10.1021/acsnano.7b06211>
- [63] Xu C, Wang L, Liu Z et al (2015) Large-area high-quality 2D ultrathin Mo<sub>2</sub>C superconducting crystals. *Nat Mater* 14:1135–1141. <https://doi.org/10.1038/nmat4374>
- [64] Tricoli A, Nasiri N, De S (2017) Wearable and miniaturized sensor technologies for personalized and preventive medicine. *Adv Func Mater* 27:1605271. <https://doi.org/10.1002/adfm.201605271>
- [65] Leonardi SG (2017) Two-dimensional zinc oxide nanostructures for gas sensor applications. *Chemosensors* 5:17. <https://doi.org/10.3390/chemosensors5020017>
- [66] Korotcenkov G, Cho BK (2013) Engineering approaches for the improvement of conductometric gas sensor parameters: part 1. Improvement of sensor sensitivity and selectivity (short survey). *Sens Actuators B Chem* 188:709–728. <https://doi.org/10.1016/j.snb.2013.07.101>
- [67] Zhou Y, Jiang Y, Xie T et al (2014) A novel sensing mechanism for resistive gas sensors based on layered reduced graphene oxide thin films at room temperature. *Sens Actuators B Chem* 203:135–142. <https://doi.org/10.1016/j.snb.2014.06.105>
- [68] Wang C, Yin L, Zhang L et al (2010) Metal oxide gas sensors: sensitivity and influencing factors. *Sensors (Basel)* 10:2088–2106. <https://doi.org/10.3390/s100302088>
- [69] Yang S, Jiang C, Wei SH (2017) Gas sensing in 2D materials. *Appl Phys Rev* 4:021304
- [70] Yuan S, Zhang S (2019) Recent progress on gas sensors based on graphene-like 2D/2D nanocomposites. *J Semicond* 40:111608–111608–111614. <https://doi.org/10.1088/1674-4926/40/11/111608>
- [71] Rout CS, Late D (2020) Fundamentals and sensing applications of 2D materials. 1st Edition. <https://www.elsevier.com/books/fundamentals-and-sensing-applications-of-2d-materials/rout/978-0-08-102577-2>. Accessed 20 Aug 2020
- [72] Rout CS (2010) Gas sensing and electrical properties of metal oxide nanostructures: nanostructures, synthesis, sensors, sensing mechanism, LEDs, FETs, carbon nanotubes, graphene. LAP LAMBERT Academic Publishing, Supercapacitors
- [73] Kumar R, Goel N, Hojaberdiiev M, Kumar M (2020) Transition metal dichalcogenides-based flexible gas sensors. *Sens Actuators A* 303:111875. <https://doi.org/10.1016/j.sna.2020.111875>
- [74] Tyagi D, Wang H, Huang W et al (2020) Recent advances in two-dimensional-material-based sensing technology toward health and environmental monitoring applications. *Nanoscale* 12:3535–3559. <https://doi.org/10.1039/C9NR10178K>
- [75] Yue Q, Shao Z, Chang S, Li J (2013) Adsorption of gas molecules on monolayer MoS<sub>2</sub> and effect of applied electric field. *Nanoscale Res Lett* 8:425. <https://doi.org/10.1186/1556-276X-8-425>
- [76] Qiao X-Q, Zhang Z-W, Hou D-F et al (2018) Tunable MoS<sub>2</sub>/SnO<sub>2</sub> P-N heterojunctions for an efficient trimethylamine gas sensor and 4-nitrophenol reduction catalyst. *ACS Sustain Chem Eng* 6:12375–12384. <https://doi.org/10.1021/acssuschemeng.8b02842>
- [77] Zhang D, Xu Z, Yang Z, Song X (2020) High-performance flexible self-powered tin disulfide nanoflowers/reduced graphene oxide nanohybrid-based humidity sensor driven by triboelectric nanogenerator. *Nano Energy* 67:104251. <https://doi.org/10.1016/j.nanoen.2019.104251>
- [78] Sun Q, Wang J, Hao J et al (2019) SnS<sub>2</sub>/SnS p–n heterojunctions with an accumulation layer for ultrasensitive room-temperature NO<sub>2</sub> detection. *Nanoscale* 11:13741–13749. <https://doi.org/10.1039/C9NR02780G>
- [79] Tang H, Li Y, Sokolovskij R et al (2019) Ultra-high sensitive NO<sub>2</sub> gas sensor based on tunable polarity transport in CVD-WS<sub>2</sub>/IGZO p–n heterojunction. *ACS Appl Mater Interfaces* 11:40850–40859. <https://doi.org/10.1021/acsmami.9b13773>
- [80] Sharma S, Kumar A, Singh N, Kaur D (2018) Excellent room temperature ammonia gas sensing properties of n-MoS<sub>2</sub>/p-CuO heterojunction nanoworms. *Sens Actuators*

- B Chem 275:499–507. <https://doi.org/10.1016/j.snb.2018.08.046>
- [81] Liu L, Ikram M, Ma L et al (2020) Edge-exposed MoS<sub>2</sub> nanospheres assembled with SnS<sub>2</sub> nanosheet to boost NO<sub>2</sub> gas sensing at room temperature. J Hazard Mater 393:122325. <https://doi.org/10.1016/j.jhazmat.2020.122325>
- [82] Wang H, Zhang L, Chen Z et al (2014) Semiconductor heterojunction photocatalysts: design, construction, and photocatalytic performances. Chem Soc Rev 43:5234–5244. <https://doi.org/10.1039/C4CS00126E>
- [83] Liu YJ, Hao LZ, Gao W et al (2015) Growth and humidity-dependent electrical properties of bulk-like MoS<sub>2</sub> thin films on Si. RSC Adv 5:74329–74335. <https://doi.org/10.1039/C5RA11454C>
- [84] Liu Y, Hao L, Gao W et al (2015) Electrical characterization and ammonia sensing properties of MoS<sub>2</sub>/Si p–n junction. J Alloy Compd 631:105–110. <https://doi.org/10.1016/j.jallcom.2015.01.111>
- [85] Zhao S, Xue J, Kang W (2014) Gas adsorption on MoS<sub>2</sub> monolayer from first-principles calculations. Chem Phys Lett 595–596:35–42. <https://doi.org/10.1016/j.cplett.2014.01.043>
- [86] Zhang D, Jin Y, Cao Y (2018) Facile synthesis and ammonia gas sensing properties of NiO nanoparticles decorated MoS<sub>2</sub> nanosheets heterostructure. J Mater Sci Mater Electron. <https://doi.org/10.1007/s10854-018-0323-3>
- [87] Feng Z, Chen B, Qian S et al (2016) Chemical sensing by band modulation of a black phosphorus/molybdenum diselenide van der Waals hetero-structure. 2D Mater 3:035021. <https://doi.org/10.1088/2053-1583/3/3/035021>
- [88] Liu B, Chen L, Liu G et al (2014) High-performance chemical sensing using schottky-contacted chemical vapor deposition grown monolayer MoS<sub>2</sub> transistors. ACS Nano 8:5304–5314. <https://doi.org/10.1021/nn5015215>
- [89] Yang J, Kwak H, Lee Y et al (2016) MoS<sub>2</sub>–InGaZnO heterojunction phototransistors with broad spectral responsivity. ACS Appl Mater Interfaces 8:8576–8582. <https://doi.org/10.1021/acsami.5b11709>
- [90] Wang Y, Zhou Y, Ren H et al (2020) Room-temperature and humidity-resistant trace nitrogen dioxide sensing of few-layer black phosphorus nanosheet by incorporating zinc oxide nanowire. Anal Chem 92:11007–11017. <https://doi.org/10.1021/acs.analchem.9b05623>
- [91] Huang Y, Jiao W, Chu Z et al (2020) High sensitivity, humidity-independent, flexible NO<sub>2</sub> and NH<sub>3</sub> gas sensors based on SnS<sub>2</sub> Hybrid functional graphene ink. ACS Appl Mater Interfaces 12:997–1004. <https://doi.org/10.1021/acsami.9b14952>
- [92] Wang X, Gu D, Li X et al (2019) Reduced graphene oxide hybridized with WS<sub>2</sub> nanoflakes based heterojunctions for selective ammonia sensors at room temperature. Sens Actuators B Chem 282:290–299. <https://doi.org/10.1016/j.snb.2018.11.080>
- [93] Huang Y, Jiao W, Chu Z et al (2019) Ultrasensitive room temperature ppb-level NO<sub>2</sub> gas sensors based on SnS<sub>2</sub>/rGO nanohybrids with P-N transition and optoelectronic visible light enhancement performance. J Mater Chem C 7:8616–8625. <https://doi.org/10.1039/C9TC02436K>
- [94] Abdollahi H, Samkan M, Hashemi MM (2019) Fabrication of rGO nano-sheets wrapped on Ni doped ZnO nanowire p–n heterostructures for hydrogen gas sensing. New J Chem 43:19253–19264. <https://doi.org/10.1039/C9NJ05152J>
- [95] Zhao PX, Tang Y, Mao J et al (2016) One-dimensional MoS<sub>2</sub>-decorated TiO<sub>2</sub> nanotube gas sensors for efficient alcohol sensing. J Alloy Compd 674:252–258. <https://doi.org/10.1016/j.jallcom.2016.03.029>
- [96] Pargoletti E, Hossain UH, Bernardo ID et al (2019) Room-temperature photodetectors and VOC sensors based on graphene oxide–ZnO nano-heterojunctions. Nanoscale 11:22932–22945. <https://doi.org/10.1039/C9NR08901B>
- [97] Guo D, Cai P, Sun J et al (2016) Reduced-graphene-oxide/metal-oxide p-n heterojunction aerogels as efficient 3D sensing frameworks for phenol detection. Carbon 99:571–578. <https://doi.org/10.1016/j.carbon.2015.12.074>
- [98] Li X, Wang Y, Tian W, Cao J (2019) Graphitic carbon nitride nanosheets decorated flower-like NiO composites for high-performance triethylamine detection. ACS Omega 4:9645–9653. <https://doi.org/10.1021/acsomega.9b00905>
- [99] Andre RS, Mercante LA, Facure MHM et al (2019) Enhanced and selective ammonia detection using In<sub>2</sub>O<sub>3</sub>/reduced graphene oxide hybrid nanofibers. Appl Surf Sci 473:133–140. <https://doi.org/10.1016/j.apsusc.2018.12.101>
- [100] Schedin F, Geim AK, Morozov SV et al (2007) Detection of individual gas molecules adsorbed on graphene. Nat Mater 6:652–655. <https://doi.org/10.1038/nmat1967>
- [101] Yaghouti Niyat F, Shahrokh Abadi MH (2018) COMSOL-based modeling and simulation of SnO<sub>2</sub>/rGO gas sensor for detection of NO<sub>2</sub>. Sci Rep 8:2149. <https://doi.org/10.1038/s41598-018-20501-2>
- [102] Russo PA, Donato N, Leonardi SG et al (2012) Room-temperature hydrogen sensing with heteronanostructures based on reduced graphene oxide and tin oxide. Angew Chem Int Ed Engl 51:11053–11057. <https://doi.org/10.1002/anie.201204373>
- [103] Basu S, Bhattacharyya P (2012) Recent developments on graphene and graphene oxide based solid state gas sensors. Sens Actuators B Chem 173:1–21. <https://doi.org/10.1016/j.snb.2012.07.092>

- [104] Kamble V (2019) Facile and in-situ spray deposition of SnO<sub>2</sub> – reduced graphene oxide heterostructure sensor devices. *J Phys Commun.* <https://doi.org/10.1088/2399-6528/aafe35>
- [105] Zou C, Hu J, Su Y et al (2019) Three-dimensional Fe<sub>3</sub>O<sub>4</sub>@reduced graphene oxide heterojunctions for high-performance room-temperature NO<sub>2</sub> sensors. *Front Mater* 6:195. <https://doi.org/10.3389/fmats.2019.00195>
- [106] Liu X, Sun J, Zhang X (2015) Novel 3D graphene aerogel–ZnO composites as efficient detection for NO<sub>2</sub> at room temperature. *Sens Actuators B Chem* 211:220–226. <https://doi.org/10.1016/j.snb.2015.01.083>
- [107] Yan C, Lu H, Gao J et al (2018) Improved NO<sub>2</sub> sensing properties at low temperature using reduced graphene oxide nanosheet–In<sub>2</sub>O<sub>3</sub> heterojunction nanofibers. *J Alloy Compd* 741:908–917. <https://doi.org/10.1016/j.jallcom.2018.01.209>
- [108] Bhati VS, Sheela D, Roul B et al (2019) NO<sub>2</sub> gas sensing performance enhancement based on reduced graphene oxide decorated V<sub>2</sub>O<sub>5</sub> thin films. *Nanotechnology* 30:224001. <https://doi.org/10.1088/1361-6528/ab0321>
- [109] Murali G, Reddeppa M, Seshendra Reddy Ch et al (2020) Enhancing the charge carrier separation and transport via nitrogen-doped graphene quantum dot-TiO<sub>2</sub> nanoplate hybrid structure for an efficient NO gas sensor. *ACS Appl Mater Interfaces* 12:13428–13436. <https://doi.org/10.1021/acsami.9b19896>
- [110] Ma L, Zhang X, Wang J et al (2020) Controllable synthesis of an intercalated SnS<sub>2</sub>/aEG structure for enhanced NO<sub>2</sub> gas sensing performance at room temperature. *New J Chem* 44:8650–8659. <https://doi.org/10.1039/D0NJ01005G>
- [111] Li Q, Cen Y, Huang J et al (2018) Zinc oxide–black phosphorus composites for ultrasensitive nitrogen dioxide sensing. *Nanoscale Horiz* 3:525–531. <https://doi.org/10.1039/C8NH00052B>
- [112] Tammanoon N, Wisitsoraat A, Sriprachuabwong C et al (2015) Ultrasensitive NO<sub>2</sub> sensor based on ohmic metal–semiconductor interfaces of electrolytically exfoliated graphene/flame-spray-made SnO<sub>2</sub> nanoparticles composite operating at low temperatures. *ACS Appl Mater Interfaces* 7:24338–24352. <https://doi.org/10.1021/acsami.5b09067>
- [113] Han Y, Huang D, Ma Y et al (2018) Design of hetero-nanostructures on MoS<sub>2</sub> nanosheets to boost NO<sub>2</sub> room-temperature sensing. *ACS Appl Mater Interfaces* 10:22640–22649. <https://doi.org/10.1021/acsami.8b05811>
- [114] Han Y, Ma Y, Liu Y et al (2019) Construction of MoS<sub>2</sub>/SnO<sub>2</sub> heterostructures for sensitive NO<sub>2</sub> detection at room temperature. *Appl Surf Sci* 493:613–619. <https://doi.org/10.1016/j.apsusc.2019.07.052>
- [115] Zhao S, Wang G, Liao J et al (2018) Vertically aligned MoS<sub>2</sub>/ZnO nanowires nanostructures with highly enhanced NO<sub>2</sub> sensing activities. *Appl Surf Sci* 456:808–816. <http://doi.org/10.1016/j.apsusc.2018.06.103>
- [116] Jaiswal J, Sanger A, Tiwari P, Chandra R (2020) MoS<sub>2</sub> hybrid heterostructure thin film decorated with CdTe quantum dots for room temperature NO<sub>2</sub> gas sensor. *Sens Actuators B Chem* 305:127437. <https://doi.org/10.1016/j.snb.2019.127437>
- [117] Jha RK, Wan M, Jacob C, Guha PK (2017) Ammonia vapour sensing properties of in situ polymerized conducting PANI-nanofiber/WS<sub>2</sub> nanosheet composites. *New J Chem* 42:735–745. <https://doi.org/10.1039/C7NJ0334E>
- [118] Zhou Y, Gao C, Guo Y (2018) UV assisted ultrasensitive trace NO<sub>2</sub> gas sensing based on few-layer MoS<sub>2</sub> nanosheet–ZnO nanowire heterojunctions at room temperature. *J Mater Chem A* 6:10286–10296. <https://doi.org/10.1039/C8TA02679C>
- [119] Tang H, Tan C, Yang H et al (2019) Tunable electronic and optical properties of the WS<sub>2</sub>/IGZO heterostructure via an external electric field and strain: a theoretical study. *Phys Chem Chem Phys* 21:14713–14721. <https://doi.org/10.1039/C9CP02084E>
- [120] Deng Y, Luo Z, Conrad NJ et al (2014) Black phosphorus-monolayer MoS<sub>2</sub> van der Waals heterojunction p–n diode. *ACS Nano* 8:8292–8299. <https://doi.org/10.1021/nn5027388>
- [121] Miao J, Xu Z, Li Q et al (2017) Vertically stacked and self-encapsulated van der waals heterojunction diodes using two-dimensional layered semiconductors. *ACS Nano* 11:10472–10479. <https://doi.org/10.1021/acsnano.7b05755>
- [122] Ye L, Li H, Chen Z, Xu J (2016) Near-infrared photodetector based on MoS<sub>2</sub>/black phosphorus heterojunction. *ACS Photonics* 3:692–699. <https://doi.org/10.1021/acspophotonics.6b00079>
- [123] Lee Y, Um D-S, Lim S et al (2019) Gate-tunable and programmable n-InGaAs/black phosphorus heterojunction diodes. *ACS Appl Mater Interfaces* 11:23382–23391. <https://doi.org/10.1021/acsami.9b07701>
- [124] Srivastava PK, Hassan Y, Gebredingle Y et al (2019) Van der Waals broken-Gap p–n heterojunction tunnel diode based on black phosphorus and rhodium disulfide. *ACS Appl Mater Interfaces* 11:8266–8275. <https://doi.org/10.1021/acsami.8b22103>
- [125] Jeon PJ, Lee YT, Lim JY et al (2016) Black phosphorus–zinc oxide nanomaterial heterojunction for p–n diode and junction field-effect transistor. *Nano Lett* 16:1293–1298. <https://doi.org/10.1021/acs.nanolett.5b04664>
- [126] Chen R, Lin C, Yu H et al (2016) Templating C<sub>60</sub> on MoS<sub>2</sub> nanosheets for 2D Hybrid van der Waals p–n

- nanoheterojunctions. *Chem Mater* 28:4300–4306. <https://doi.org/10.1021/acs.chemmater.6b01115>
- [127] Zhang K, Peng M, Wu W et al (2017) A flexible p-CuO/n-MoS<sub>2</sub> heterojunction photodetector with enhanced photoresponse by the piezo-phototronic effect. *Mater Horiz* 4:274–280. <https://doi.org/10.1039/C6MH00568C>
- [128] Xue F, Yang L, Chen M et al (2017) Enhanced photoresponsivity of the MoS<sub>2</sub>-GaN heterojunction diode via the piezo-phototronic effect. *NPG Asia Materials* 9:e418–e418. <https://doi.org/10.1038/am.2017.142>
- [129] Li P, Yuan K, Lin D-Y et al (2019) p-MoS<sub>2</sub>/n-InSe van der Waals heterojunctions and their applications in all-2D optoelectronic devices. *RSC Adv* 9:35039–35044. <https://doi.org/10.1039/C9RA06667E>
- [130] Jariwala D, Howell SL, Chen K-S et al (2016) Hybrid, gate-tunable, van der Waals p-n Heterojunctions from pentacene and MoS<sub>2</sub>. *Nano Lett* 16:497–503. <https://doi.org/10.1021/acs.nanolett.5b04141>
- [131] Kim J-K, Cho K, Kim T-Y et al (2016) Trap-mediated electronic transport properties of gate-tunable pentacene/MoS<sub>2</sub> p-n heterojunction diodes. *Sci Rep* 6:36775. <http://doi.org/10.1038/srep36775>
- [132] Fang C, Wang H, Shen Z et al (2019) High-performance photodetectors based on lead-free 2D ruddlesden-popper perovskite/MoS<sub>2</sub> heterostructures. *ACS Appl Mater Interfaces* 11:8419–8427. <https://doi.org/10.1021/acsami.8b20538>
- [133] Wang L, Jie J, Shao Z et al (2015) MoS<sub>2</sub>/Si heterojunction with vertically standing layered structure for ultrafast, high-detectivity, self-driven visible-near infrared photodetectors. *Adv Func Mater* 25:2910–2919. <https://doi.org/10.1002/adfm.201500216>
- [134] Um D-S, Lee Y, Lim S et al (2016) High-performance MoS<sub>2</sub>/CuO nanosheet-on-one-dimensional heterojunction photodetectors. *ACS Appl Mater Interfaces* 8:33955–33962. <https://doi.org/10.1021/acsami.6b12574>
- [135] Miao J, Liu X, Jo K et al (2020) Gate-tunable semiconductor heterojunctions from 2D/3D van der Waals interfaces. *Nano Lett* 20:2907–2915
- [136] Tan D, Wang X, Zhang W et al (2018) Carrier transport and photoresponse in GeSe/MoS<sub>2</sub> heterojunction p-n diodes. *Small* 14:e1704559. <https://doi.org/10.1002/smll.201704559>
- [137] Pezeshki A, Shokouh SHH, Nazari T et al (2016) Electric and photovoltaic behavior of a few-layer  $\alpha$ -MoTe<sub>2</sub>/MoS<sub>2</sub> dichalcogenide heterojunction. *Adv Mater Weinheim* 28:3216–3222. <https://doi.org/10.1002/adma.201504090>
- [138] Cheng R, Li D, Zhou H et al (2014) Electroluminescence and photocurrent generation from atomically sharp WSe<sub>2</sub>/MoS<sub>2</sub> heterojunction p-n diodes. *Nano Lett* 14:5590–5597. <https://doi.org/10.1021/nl502075n>
- [139] Jia S, Jin Z, Zhang J et al (2020) Lateral monolayer MoSe<sub>2</sub>-WSe<sub>2</sub> p-n heterojunctions with giant built-in potentials. *Small*. <https://doi.org/10.1002/smll.202002263>
- [140] Lee HS, Choi K, Kim JS et al (2017) Coupling two-dimensional MoTe<sub>2</sub> and InGaZnO thin-film materials for hybrid PN junction and CMOS inverters. *ACS Appl Mater Interfaces* 9:15592–15598. <https://doi.org/10.1021/acsami.7b02838>
- [141] Ahn J, Kang J-H, Kyhm J et al (2020) Self-powered visible-invisible multiband detection and imaging achieved using high-performance 2D MoTe<sub>2</sub>/MoS<sub>2</sub> semivertical heterojunction photodiodes. *ACS Appl Mater Interfaces* 12:10858–10866. <https://doi.org/10.1021/acsami.9b22288>
- [142] Kumar GM, Xiao F, Ilanchezhian P et al (2016) Enhanced photoelectrical performance of chemically processed SnS<sub>2</sub> nanoplates. *RSC Adv* 6:99631–99637. <https://doi.org/10.1039/C6RA20491K>
- [143] Serna MI, Hasan SMN, Nam S et al (2018) Low-temperature deposition of layered SnSe<sub>2</sub> for heterojunction diodes. *Adv Mater Interfaces* 5:1800128. <https://doi.org/10.1002/admi.201800128>
- [144] Dastgeer G, Khan MF, Nazir G et al (2018) Temperature-dependent and gate-tunable rectification in a black phosphorus/WS<sub>2</sub> van der Waals heterojunction diode. *ACS Appl Mater Interfaces* 10:13150–13157. <https://doi.org/10.1021/acsami.8b00058>
- [145] Lee S, Lee HS, Yu S et al (2020) Tungsten dichalcogenide nanoflake/InGaZnO thin-film heterojunction for photodetector, inverter, and AC rectifier circuits. *Adv Electron Mater* 6:2000026. <https://doi.org/10.1002/aelm.202000026>
- [146] Wu E, Wu D, Jia C et al (2019) In situ fabrication of 2D WS<sub>2</sub>/Si type-II heterojunction for self-powered broadband photodetector with response up to mid-infrared. *ACS Photonics* 6:565–572. <https://doi.org/10.1021/acspophotonics.8b01675>
- [147] Li D, Wang B, Chen M et al (2017) Gate-controlled BP-WSe<sub>2</sub> heterojunction diode for logic rectifiers and logic optoelectronics. *Small* 13:1603726. <https://doi.org/10.1002/smll.201603726>
- [148] Lee YT, Jeon PJ, Han JH et al (2017) Mixed-dimensional 1D ZnO–2D WSe<sub>2</sub> van der Waals heterojunction device for photosensors. *Adv Func Mater* 27:1703822. <https://doi.org/10.1002/adfm.201703822>
- [149] Liu H, Zhu X, Sun X et al (2019) Self-powered broad-band photodetectors based on vertically stacked WSe<sub>2</sub>/Bi<sub>2</sub>Te<sub>3</sub> p-n heterojunctions. *ACS Nano* 13:13573–13580. <https://doi.org/10.1021/acsnano.9b07563>

- [150] Varghese A, Saha D, Thakar K et al (2020) Near-direct bandgap WSe<sub>2</sub>/ReS<sub>2</sub> type-II pn heterojunction for enhanced ultrafast photodetection and high-performance photovoltaics. *Nano Lett* 20:1707–1717. <https://doi.org/10.1021/acs.nanolett.9b04879>
- [151] Murali K, Dandu M, Das S, Majumdar K (2018) Gate-tunable WSe<sub>2</sub>/SnSe<sub>2</sub> backward diode with ultrahigh-reverse rectification ratio. *ACS Appl Mater Interfaces* 10:5657–5664. <https://doi.org/10.1021/acsami.7b18242>
- [152] Dutta D, Hazra SK, Das J et al (2015) Studies on p-TiO<sub>2</sub>/n-graphene heterojunction for hydrogen detection. *Sens Actuators B Chem* 212:84–92. <https://doi.org/10.1016/j.snb.2015.02.009>
- [153] Zhou Y, Liu G, Zhu X, Guo Y (2017) Ultrasensitive NO<sub>2</sub> gas sensing based on rGO/MoS<sub>2</sub> nanocomposite film at low temperature. *Sens Actuators B Chem* 251:280–290. <https://doi.org/10.1016/j.snb.2017.05.060>
- [154] Reddeppa M, Park B-G, Murali G et al (2020) NO<sub>x</sub> gas sensors based on layer-transferred n-MoS<sub>2</sub>/p-GaN heterojunction at room temperature: study of UV light illuminations and humidity. *Sens Actuators B Chem* 308:127700. <https://doi.org/10.1016/j.snb.2020.127700>
- [155] Jana A, Kumari K, Dey A et al (2019) Fabrication of P-N heterojunction based MoS<sub>2</sub> modified CuPc nanoflowers for humidity sensing. *Sens Actuators A* 299:111574. <https://doi.org/10.1016/j.sna.2019.111574>
- [156] Li X, Zhou Y, Tai H et al (2020) Nanocomposite films of p-type MoS<sub>2</sub> nanosheets/n-type ZnO nanowires: sensitive and low-temperature ppb-level NO<sub>2</sub> detection. *Mater Lett* 262:127148. <https://doi.org/10.1016/j.matlet.2019.127148>

**Publisher's Note** Springer Nature remains neutral with regard to jurisdictional claims in published maps and institutional affiliations.